Exploring the Sensitivity of Lunar Interior Structure from Geophysical and Geochemical Constraints

H. Fuqua Haviland[1*], P. M. Bremner[1*], A. Mallik[3,4*], M. R. Diamond[5*], S. Panovska[6], S. J. Lock[7]

[1]Heliophysics and Planetary Science Branch, Marshall Space Flight Center.

[3]Bayerisches Geoinstitut, University of Bayreuth, Bayreuth, Germany.

[4]Department of Geosciences, University Arizona.

[5]Earth and Planetary Science Department, University of California, Berkeley.

[6]GFZ Helmholtz-Zentrum Potsdam.

[7]Division of Geological and Planetary Sciences, California Institute of Technology.

Corresponding author: Heidi Fuqua Haviland (heidi.haviland@nasa.gov)

**These authors contributed equally.*

Key Points:

- Joint geophysical and geochemical analysis places constraints on lunar interior structure, including core size and ilmenite-bearing volume within the mantle.
- Elastic properties are calculated for multiphase minerals enabling a wide range of temperature and composition constraints to be self-consistently explored.
- A compositionally homogeneous lunar mantle is likely only possible with elevated mantle temperatures.

Abstract

The key to evaluating the formation history and evolution of the Moon lies in understanding the current state of its interior. We used a multidisciplinary approach to explore the current day lunar structure and composition with the aim of identifying signatures of formation and early evolution. We constructed a large number of 1D lunar interior models to explore a wide range of potential structures and identified those models that match the present-day mass, moment of inertia, and bulk silicate composition of the Moon. In an advance on previous studies, we explicitly calculate the physical and elastic properties of the varying mineral assemblages in the lunar interior using multicomponent equations of state. We considered models with either a compositionally homogeneous mantle or a stratified mantle that preserved remnants of magma ocean crystallization, and tested thermal profiles that span the range of proposed selenotherms. For the models that reproduced the observed mass and moment of inertia, we found a narrow range of possible metallic (iron) core radii (269-387 km) consistent with previous determinations. We explored the possibility of an ilmenite bearing layer both below the crust and at the core-mantle boundary as a potential tracer of magma ocean solidification and overturn. We observed a trade-off between the mass of the upper and lower ilmenite-bearing layers and structures that have undergone mantle overturn are both consistent with present observations.

Plain Language Summary

In order to understand how the Moon formed, along with the following history including the processes that change and shape it, the current state of the lunar interior offers a lot of valuable information or clues. We used several different computer simulation tools from different disciplines to calculate the Moon's interior structure. We then compared our calculations with observations of the Moon's mass and moment of inertia (a measure of how its weight is distributed through the interior) and the average composition and chemistry of the Moon. We considered a Moon that is well mixed and one that has preserved layers from its early history and tried different temperature structures. We find that the Moon has to have a small dense iron core and that it may have a hot soft layer just above the core that can dampen moonquakes.

Table of Contents:

1. Introduction

Studying the current state of the Moon's interior structure is critical to unlocking its past, including its formation (Jaumann et al., 2012; Yang & Zhao, 2015) and thermal and tidal evolution (Ćuk et al., 2016; Ćuk & Stewart, 2012; Tian et al., 2017; Wisdom & Tian, 2015; Touma & Wisdom, 1994). Despite considerable effort to constrain the physical and geochemical properties of the lunar interior, prominent open questions remain, including the possible existence of a lower mantle partial-melt layer; the precise size, state, and composition of the core; and the consequence and evolution of crystallization of the magma ocean (MO) (Garcia et al., 2011, 2012; Khan et al., 2013; Neal, 2009; Stevenson & Halliday, 2014; Weber et al., 2011; Wieczorek et al., 2006). These phenomena have geophysical and geochemical implications for lunar evolution and are explored in this paper.

A variety of independent geophysical methods have provided key insights to our understanding of the Moon's interior structure. Analyses of Apollo seismograms have found a differentiated lunar interior with a small dense iron core (Garcia et al., 2011, 2012; Lognonné & Johnson, 2007; Nakamura et al., 1978; Weber et al., 2011). The lower degree observations of mass; moment of inertia (MOI); and tidal Love numbers, k2 and h2; place rough constraints on the global stratigraphy of the Moon (e.g., Williams et al., 2001, 2014). The existence of a lunar core is consistent with the strong magnetic fields measured in lunar rocks (Shea et al., 2012; Tikoo et al., 2014; Weiss & Tikoo, 2014; Tikoo et al., 2017; Evans et al., 2018) which suggest at least part of a metallic core was once molten. A partially molten layer at the core-mantle boundary (CMB) has been suggested to explain the lack of observed far-side quakes (Nakamura et al., 1973; Nakamura, 2005), the observation of weak reflected phases from deep moonquakes (Weber et al., 2011), and the dissipation of tidal energy within the deep interior (Harada et al., 2014; Williams et al., 2001). Gravity and topography measurements, from GRAIL and LRO, have constrained the average crustal thickness to be ~40 km (Wieczorek et al., 2013).

Analysis of lunar meteorites and samples returned by the Apollo missions have been used to constrain the chemical structure and bulk composition of the Moon (e.g., Ringwood, 1979; Taylor, 1982). It is inferred that the Moon was once at least partially molten and that the magma ocean MO fractionally crystallized to form an olivine-pyroxene rich mantle, a plagioclase floatation crust, and a potential iron- and titanium-rich (Fe+Ti-rich), or equivalently ilmenite-bearing, sub-crustal layer which has been proposed to form during the final stages (i.e., the last ~5%) of the MO crystallization (Charlier et al., 2018; Elardo et al., 2011; Elkins-Tanton et al.,

2011; Lin et al., 2017a, 2017b; Snyder et al., 1992). One proposed origin of the partially molten basal mantle layer is that a portion of a sub-crustal ilmenite-bearing layer that formed during MO solidification sank to the CMB due to its higher density relative to the surrounding mantle (e.g., Dygert et al., 2016; Hess & Parmentier, 1995; Li et al., 2019; Yu et al., 2019; Zhong et al., 2000). Sinking of such an ilmenite-bearing layer into the deep lunar mantle is supported from multiple saturation studies of Fe+Ti-rich picritic red, black, and orange glasses from Apollo 12, 14, and 17, respectively. These experiments suggest that the glasses were sourced from depths of 300-500 km (Brown & Grove, 2015; Elkins Tanton et al., 2002; Krawczynski & Grove, 2012). This implies that ilmenite-bearing heterogeneities exist at depths within the lunar mantle, contradicting the sequence predicted by MO fractional crystallization models unless this subcrustal layer sank deep into the lunar mantle caused by a mantle overturn event. The ilmenite-bearing layer is likely enriched in heat-producing incompatible elements such as K, U and Th (Jolliff et al., 2000) and has a lower solidus temperature than magnesian, olivine, and peridotite (the potential compositions of the lunar lower mantle). Hence, a partially molten basal mantle layer could result from the presence of ilmenite-bearing heterogeneities at the CMB (Mallik et al., 2019; Yao & Liang, 2012) and emplaced by overturn.

The aim of this paper is to explore the structure of the present-day lunar interior using combined geochemical and geophysical models. We constructed a large number of 1D lunar interior models to explore a wide range of potential structures and identified those models that match the present-day mass, moment of inertia, and bulk silicate composition of the Moon. In an advance on previous studies, we explicitly calculate the physical and elastic properties of the varying mineral assemblages in the lunar interior using multicomponent equations of state.To do this, we have constructed a novel routine, *Selenoman,* which uses the BurnMan [Cottaar et al., 2014, 2016] algorithm to calculate the properties of mineral assemblages within the pressure and temperature range of the lunar interior. To constrain the range of plausible interior structure models, we combine estimates of the bulk lunar composition derived from Apollo samples with GRAIL measurements of mass and MOI. Our approach provides the first self-consistent mineral physics calculations of the lunar interior and explores a wide range of possible compositions and temperature profiles, or selenotherms. Our interdisciplinary approach allows us to assess the sensitivity of the lunar interior to composition and temperature and the consequences of a full range of possible crystallization scenarios and subsequent mantle evolution. In particular, we consider the existence of ilmenite-bearing layers at the bottom and/or top of the mantle as a

probe of the efficiency of mantle overturn during or after mantle solidification, as the presence of an ilmenite-bearing basal mantle layer provides suggestive evidence of mantle overturn.

Section 2 provides a background of previous lunar geophysical analyses which motivate this project. In Section 3, we present the methods used to construct simplified 1D radial compositional models informed by thermoelastic constraints of phase equilibria, and describe the search methods used for exploring the range of potential lunar structures. Our results are presented in Section 4 and discussed in Section 5. Lastly, our conclusions are summarized in Section 6. A glossary of key terms along with additional figures and text is provided in the supplementary materials.

2. Background

We review the current state of knowledge of the lunar interior, concentrating on the core and partial melt layer.

The presence of a small, dense metallic core has been demonstrated by several studies. These include a compositional modeling analysis by Yan et al. (2015) suggesting that the most plausible lunar core radius and density are 370 km and5.0×10^3 kg/m^3, respectively, for a three-layer (crust, mantle, core) model using a Monte Carlo method constrained by mean MOI, mantle density, crustal thickness and density. This radius is consistent with the inference of a metallic core of radius 340 ± 90 km by electromagnetic sounding observations (Hood et al., 1999; Shimizu et al., 2013) and with size estimates from seismic observations of an iron alloy (Garcia et al. 2011, 2012). Weber et al. (2011) infer a differentiated core with a solid inner core of radius 240 ± 10 km and density 8.0×10^3kg/m^3, and a less dense fluid outer core with a 330 ± 20 km radius containing less than 6% light elements. Apollo samples show that the lunar magnetic dynamo produced surface fields of ~50 μT between approximately 4.25 - 3.56 Ga (Laneuville et al., 2014, 2018; Shea et al., 2012; Tikoo et al., 2014; Weiss & Tikoo, 2014), and continued in a weakened state (< ~5 μT) until ~2.5 Ga, possibly powered by a secondary mechanism (Tikoo et al., 2017). However, a recent analysis shows lunar core convection alone does not produce enough energy to sustain a dynamo for longer than 28 Myr (Evans et al., 2018), thus, the mechanism for dynamo generation meeting the observed magnitude and duration is currently unknown.

The existence and origin of a partially molten layer above the CMB has not reached a consensus. This layer would inhibit core cooling (Stegman et al., 2003, Harada et al., 2014) and have implications for global thermal evolution of the planet (e.g., Laneuville et al., 2018). In

addition, the high temperatures required to maintain a partially molten layer pose a challenge to our current understanding of the brittle-ductile fault source mechanism of the deep moonquakes (Kawamura et al., 2017). Weber et al. (2011) inferred that the existence of such a layer is based on the observation of reflections from deep moonquakes showing a seismically distinct layer near the CMB with slow S-wave velocity, indicative of the presence of partial melt. Nimmo et al. (2012), however, modelled the tidal response of potential lunar interior structures and conclude that melt is not necessary to explain the observed dissipation factor and tidal Love numbers of the Moon, and that dissipation due to elevated CMB temperatures alone is sufficient to match the observations. In contrast, Khan et al. (2014) reasserted that a deep mantle partial melt layer likely exists based on joint inversions of electrical conductivity, seismic, MOI, and mass observations. Harada et al. (2014) use viscoelastic tidal simulations and geodetic observations to constrain the viscosity of this layer to be extremely low (2×10^{16} Pa s) and found that tidal dissipation is concentrated in this layer. Matsuyama et al. (2016) took a Bayesian approach to invert for a five-layer interior structure model and found no conclusive evidence for a low rigidity transition layer at the CMB. The contrasting conclusions of previous studies demonstrate the need for further investigation of the existence and geophysical properties of a rheologically and seismically distinct. Moreover, the core and interior layers will have geophysical and chemical signatures that can be observed and tested.

3. Methodology: Current-day lunar internal structure constraints from Mass, MOI, and Bulk Composition

In order to constrain the present-day structure of the lunar interior, we generated an ensemble of candidate compositions that were tested for viability. First, we constructed three different geochemically-informed models of the lunar interior stratigraphy consisting of layers of distinct mineralogical assemblages. Next, we calculated the geophysical and geochemical over different combinations of thicknesses of each of the stratigraphic layers and compared the resulting lunar structure models to observational constraints. For each model, we calculated physical material properties based on the radial profiles of mineralogy and imposed temperature. In the following sections we describe these methods used to generate and assess each lunar model candidate.

Section 3.1 describes how we calculated physical mineralogical properties. Section 3.2 describes the construction of three laterally averaged 1D compositional profiles from which we

defined three model classes. We utilized three different selenotherms that span the proposed range (Section 3.3) for each model class, yielding nine total distinct model subclasses. Within each, we employed a grid search, a random sampling, and a differential evolution genetic search to locate lunar candidate compositions that are consistent with geophysical observations of the Moon (Section 3.4). Finally, we calculated the fit to the bulk chemistry as an additional, previously unutilized constraint (Section 3.5).

3.1 Selenoman: Calculation of Lunar Model Properties

To calculate material properties of composition candidate models, we have developed a new computational routine called *Selenoman* (available at https://github.com/geodynamics/burnman). Within *Selenoman*, physical parameters were forward calculated utilizing BurnMan algorithms, which we extended to include lunar mineral assemblages. *Selenoman* iteratively calculates aggregate isotropic thermoelastic moduli (properties of the composite rock) via a third-order Birch-Murnaghan thermoelastic EOS model for specified mineralogy applying the Voigt-Reuss-Hill average for multiphase assemblages. Convergence was typically achieved within five iterations.

3.2 Construction of Compositional Model Classes

The extent of mixing in the solid mantle during and after MO crystallization is uncertain (Elkins-Tanton, 2011; Maurice et al., 2017; Boukare et al., 2018; Morison et al., 2019, although there are indications that chemically heterogeneous domains exist (Brown & Grove, 2015; Elkins Tanton et al., 2002). To explore the range of possible compositional structures, we constructed three models of mantle compositional stratigraphy (Figure 1). Each model was assumed to have either a compositionally homogeneous mantle (CH; Figure 1a, b) or a compositionally stratified mantle (CS; Figure 1c). For the CH models, we considered models with two different bulk mantle compositions based on estimates of the composition of the bulk silicate Moon from Taylor (1982) (CH-T) and Hauri et al., (2015) (CH-H). In both cases we removed the contribution of the lunar crust. In both, the mantle is assumed to be well-mixed via efficient whole-mantle convection post MO crystallization. In the CS case, we assumed that a lack of vigorous whole-mantle convection preserved the MO crystallization stratigraphy until present day.

For each model, the mantle was divided into a number of mineralogically distinct layers. To investigate the possible overturn of an ilmenite-bearing layer (e.g., Elkins Tanton et al., 2002), in both CH and CS models we allowed for the existence of both upper (below the anorthositic crust) and lower (at the CMB) ilmenite-bearing layers (see Figure 1 for a description

of the mineralogy of the ilmenite-bearing layers). All three model classes included a 40 km anorthite crust, and a pure iron inner (Fe-fcc) and outer (Fe-bcc) core approximated as a fluid by setting the shear modulus to zero. The crustal thickness was fixed, but the thicknesses of all other layers varied independently (detailed in Section 3.4). The CH classes contain eight stratigraphic layers, and the CS contains ten.

3.2.1 Compositionally Homogeneous (CH)

In order to describe the mantle mineral assemblages across an isentropic selenotherm, we constructed layer compositions using the Gibbs-free energy minimization software alphaMELTS using the pMELTS calibration (Ghiorso et al., 2002) to compute equilibrium phase assemblages at isentropic decompression steps (0.005 GPa from 4 to 0.5 GPa). Given the wide range of temperature estimates at the CMB (see Section 3.3) from 730 - 1480 °C (Gagnepain-Beyneix et al., 2006; Khan et al., 2006, 2007), we chose an average value of 1250 °C as the temperature at 4 GPa, corresponding to approximately 1,010 km depth (Garcia et al., 2011, 2012). The oxygen fugacity was imposed to that of equilibrium between metallic iron and wüstite at 4 GPa, and allowed to evolve during isentropic decompression in alphaMELTS.

In each stratigraphy corresponding to a unique bulk composition (CH-H and CH-T), the mantle layers were grouped into three distinct 1D radial sections: upper, middle and lower mantle (Figure 1, Table S1). All three mantle sections contained olivine, orthopyroxene, clinopyroxene, and minor spinel. The boundary between the upper and middle sections was defined by the appearance of garnet at 1.35 GPa. The lower boundary was set to 2.0 GPa to account for the gradually shifting alphaMELTS phase assemblages at higher pressures. The phase assemblage of each layer was assumed fixed for the structure calculations, regardless of the layer's thickness.

3.2.2 Compositionally Stratified (CS)

Our CS model was constructed from two resources. First, we adopted the stratigraphy of the "MO Equilibrium + Fractional Crystallization" sequence from Snyder et al. (1992) for the upper mantle from the sub-crustal ilmenite-bearing layer to the bottom of the mid-mantle. These layers were determined by the upper mantle cumulate compositions as a function of percent MO crystallization. Second, for the lower mantle composition, we adopted the result of Elardo et al. (2011) for the composition of the cumulate pile after 50% MO crystallization of a Taylor (1982) bulk mantle.

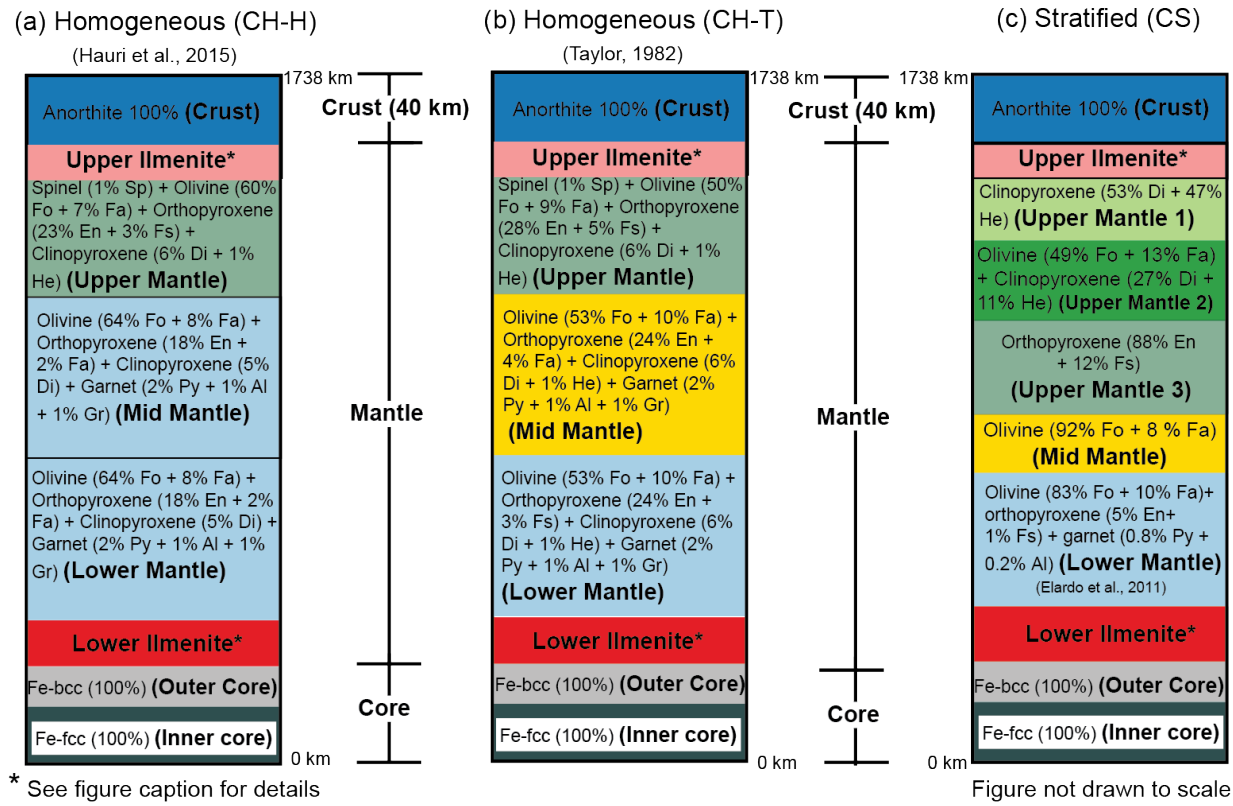

Figure 1. Lunar mantle compositional model classes: (**a**) Compositionally homogeneous Taylor (CH-T), (**b**) Compositionally homogeneous Hauri (CH-H), (**c**) Compositionally stratified (CS). The thickness of the anorthite crust is fixed, and all other layers are allowed to vary. *[Abbreviations: He - Hedenbergite, Di - Diopside, Sp - Spinel, Hc - Hercynite, Fo - Forsterite, Fa - Fayalite, En - Enstatite, Fs - Ferrosilite, Py - Pyrope, Al - Almandine, Gr - Grossular, Fe-bcc - Iron metal Body Centered Cubic, Fe-Fcc - Iron metal Face Centered Cubic]*. The mineralogy of the upper and lower ilmenite-bearing layers from Snyder et al. (1992) are: Clinopyroxene (60% He + 14% Di) + Ilmenite (23%) + Anorthite (2%).

3.3 Selenotherms: Lunar Temperature Profiles

A selenotherm is required to calculate the mineral properties (e.g., density) as a function of depth. The only direct thermal observation is from the Apollo heat flow measurements (Langseth et al., 1971, 1976), but these are point measurements on the surface that do not provide a strong constraint on the temperature at depth. Estimates of the selenotherm have been constructed using a variety of approaches including: an inversion of Apollo seismic velocities (Gagnepain-Beyneix et al., 2006), an inversion of Apollo dayside electromagnetic transfer functions (Khan et al., 2006), and a joint inversion of Apollo seismic and Lunar Prospector gravity observations (Khan et al., 2007). These profiles vary considerably and include large uncertainties (Figure 2). We therefore constructed three new selenotherms that span the range of proposed selenotherms: a hot Moon given by taking the upper bounds of published estimates at

each depth (MaxT), a cold Moon case defined by similarly taking the lower bounds (MinT), and the mean of the hot and cold cases (MeanT). For comparison, Kawamura et al. (2017) is closer to the MinT profile, while Khan et al. (2014) is closer to the MaxT profile. We extended each profile through the core by calculating a conductive thermal profile with a thermal conductivity of 30 [W/m K] (Konôpková et al., 2016; Stegman et al., 2003). Recent analysis has placed experimental constraints on the CMB temperature to be 1603-1743 K, if Fe-Ti-rich partial melt are present and neutrally buoyant (Mallik et al., 2019), which is between MeanT and MaxT. Also, another recent study based on the conductivity of hydrous olivine (Zhang et al.. 2019) proposed a CMB temperature of 1663 - 1883 K, which is closest to the MaxT profile. Each one of these individual temperature profiles is not a self-consistent selenotherm but we chose to take the extremum to explore the maximum possible effect of temperature on the inferred lunar structure. Within *Selenoman*, we imposed the three temperature profiles to each of the three compositional model classes, for a total of nine subclasses.

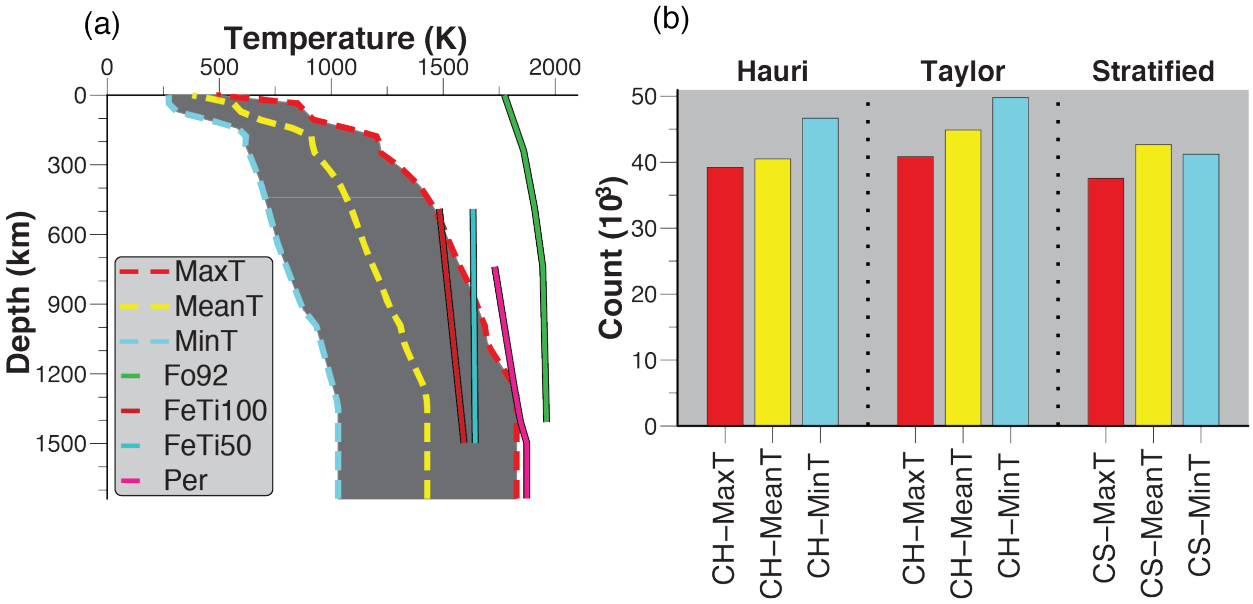

Figure 2. (**a**) Three temperature profiles are considered, bounding the proposed range of selenotherms: MaxT, MeanT, and MinT (dashed lines). The solidus curves for olivine of Forsterite 92% (Fo92, green), peridotite (Per, pink), Fe+Ti-rich ilmenite-bearing cumulates (FeTi100, red), and a mixture of 50% Fe+Ti-rich il-bearing cumulate +50% T82 mantle composition (FeTi50, cyan) (Mallik et al., 2019) are shown for reference. For each solidus curve, the P-T data are converted to depth-T via a P-profile using the model of Weber et al. (2011). (**b**) Number of models run by subclass, for a total of 383,234.

3.4 Search for Geophysically Consistent Models

For each subclass, we employed a series of search methods to find a suite of lunar candidate models consistent with observational constraints. First, we aimed to find models that could satisfy the mass (*M*) and the distribution of that mass throughout the interior (MOI) as these values are well constrained by the GRAIL mission (Williams et al., 2014; Table S3). We characterized the Mass and MOI misfit of each lunar candidate model from the reference values as a *zscore*, or the number of standard deviations ($n\sigma$) of the model *value* from the reference (*ref*) values normalized by each reported measurement error (*stderr)*:

$$zscore = n\sigma = \frac{value - ref}{stderr} \quad (8)$$

We then determined the model's overall fit to the geophysical observational constraints by calculating the root-mean-square of the (*G-RMSND* or G_{RMS}) individual *zscores* for mass and MOI:

$$G\text{-}RMSND = \left[\frac{1}{2}([zscore_{MOI}]^2 + [zscore_M]^2)\right]^{\frac{1}{2}} \quad (9)$$

New lunar candidate models were generated by varying the thickness of individual stratigraphic layers. As detailed below, we conducted the search in three stages: (1) a grid search that systematically stepped through a wide range of initial minimum and maximum thickness of each layer, (2) a random sampling of layer thickness configurations in order to "fill-in" between the steps of the coarse grid search, and (3) a differential evolution genetic search to specifically search for models with good fit to the geophysical constraints (a low *G-RMSND*). In total, we generated ~40,000 lunar compositional models per model subclass (Figure 2b).

3.4.1 Grid Search with Added Random Sampling

As a wide initial exploration of geophysical model space, we conducted a coarse grid search varying each layer's thickness over the ranges in Table 1. The intent of this initial search was to explore the full extent of the parameter space and identify structures to be used for the initialization of the differential evolution search.

The thickness of the majority of the compositional layers were allowed to range from zero to the full radial extent of the Moon minus the crust (R_L - R_{crust}). Our range of sampled lunar models allowed for both a solid inner and fluid outer core. Previous work has determined an upper bound on the radius of a dense electrically-conducting core to be ~400 km (Garcia et al., 2011, 2012; Hood et al., 1999; Shimizu et al., 2013; Weber et al., 2011; Yan et al., 2015). To be

conservative, we extended this range and sampled core sizes within 0-600 km for both inner and outer cores. We included a lower ilmenite-bearing layer ranging 0-500 km thick, which encompasses the observation made by Weber et al. (2011) of a 150 km-thick partial melt layer, assuming that a lower ilmenite-bearing layer may be responsible for the presence of partial melt near the CMB (Mallik et al., 2019). For each candidate model, the upper ilmenite-bearing layer thickness is the difference between the R_L and the sum of the other layers. We excluded stratigraphic configurations that exceeded the radius of the Moon.

Table 1. Range of layer thicknesses considered in the grid search.

Layer Names	***CH Model***		***CS Model***	
	Range (*km*)	**Increment (*km*)**	**Range (*km*)**	**Increment (*km*)**
Inner Core	0 – 600	100	0 – 600	100
Outer Core	0 – 600	100	0 – 600	100
Lower Ilmenite	0 – 500	100	0 – 500	100
Lower Mantle	0 – 1,698	200	0 – 1,698	300
Mid Mantle	0 – 1,698	200	0 – 1,698	300
Upper Mantle 3 *(CS only)*	--		0 – 1,698	300
Upper Mantle 2 *(CS only)*	--		0 – 1,698	300
Upper Mantle	0 – 1,698	200	0 – 1,698	300
Upper Ilmenite	0 – 1,698	non-uniform	0 – 1,698	non-uniform
Crust	--- constant 40 *km* (GRAIL, Wieczorek et al., 2013) ---			
Lunar Radius (R_L)	R_L = 1,738 km (Williams et al., 2014)			

We performed this grid search for all subclasses, ~10,000 models each. Since the grid search coarsely increments each layer's thickness, an additional ~10,000 candidate models per subclass were generated randomly to fill in gaps.

3.4.2 Differential Evolution

To locate the global minimum in *G-RMSND* within the prescribed model space, we employed a differential evolution (DE) optimization algorithm (Price et al., 2005). This method is a population-based stochastic function minimizer, which acts to randomly sample the parameter space through the generation of population members. DE creates and follows a path that reduces the misfit between population members and an objective function (in our case G-

RMSND). The function adds the weighted difference between two population members to a third random child vector. This method ensures that a global minimum (rather than a local minimum) is reached. In each generation, the lowest objective function is maintained. Subsequent generations are iterated until a minimum is reached. We employed a population of 15 members, with a weighting factor of 0.85 and a crossover constant of 0.9.

Similar to the grid search, we varied the thickness of all the layers with the exception of the fixed crust and the open upper ilmenite-bearing layer. The DE algorithm randomly generated and imposed layer thicknesses for all but the uppermost two stratigraphic layers (six variables for CH, and eight for CS), from the inner core through the upper mantle. DE was performed for all nine subclasses, and converged to a global minimum within 2,000 iterations for each iteration. Additional DE runs were performed as a means of verifying global minimum.

3.5 Quantifying the fit to Geochemical Constraints

As an additional constraint, we calculated the bulk composition of each model and compared this to the range of estimates of the bulk lunar composition from the literature. There is a substantial range of proposed lunar compositions and uncertainties in estimates are not typically quantified. We constructed a reference composition for the bulk silicate Moon (R_L - R_{core}) for six oxides (SiO_2, TiO_2, Al_2O_3, FeO, MgO, and CaO) by averaging the concentrations of twenty-five sets of published compositions (Table S2), assuming equal reliability (Buck & Toksoz, 1980; Delano & Lindsley, 1983; Hauri et al., 2015; Jones & Delano, 1989; Kuskov, 1997; Kuskov & Kronrod, 1998; Morgan et al., 1978; O'Neill, 1991; Ringwood et al., 1987; Ringwood, 1979; Ringwood & Kesson, 1977; Taylor, 1980, 1982, 1999; Taylor & Bence, 1975; Wänke et al., 1977; Wänke & Dreibus, 1982, 1986; Warren, 2005; Warren & Dauphas, 2014). We quantified the range in published estimates by calculating the standard deviation of each oxide concentration from the compilation of published values. Averaging estimates and calculating uncertainty in this way is not intended to produce a definitive lunar composition, but is designed to allow us to construct a quantitative metric by which we can access the consistency of our lunar structure models with the geochemical constraints.

To allow comparison with ourour models, we converted each oxide to its equivalent mass in a series of spherical shells, which we then integrated to calculate each oxide's total mass. Each sampled candidate model may possess a different total core size (sum of inner and outer core thicknesses). Therefore, we calculated both the reference and model oxide masses for a given configuration of stratigraphic thicknesses. As was done for mass and MOI, we characterized the

misfit of each oxide in mass fraction by calculating a *zscore* as defined in equation 8. From these normalized deviations, we calculated the bulk chemistry *RMSND* (*BC-RMSND* or BC_{RMS}) as:

$$BC\text{-}RMSND = \left[\frac{1}{6}\sum_i^6 \left[zscore_{oxide_i}\right]^2\right]^{\frac{1}{2}} \quad (10)$$

where the sum is over all 6 oxides. Finally, in order to quantify the qualtiy of fit considering both geochemical and geophysical constraints together, we calculated a combined geophysical and bulk composition *RMSND* (*Comb-RMSND* or $Comb_{RMS}$ or $G+BC_{RMS}$):

$$Comb\text{-}RMSND = \left[\frac{1}{2}([G\text{-}RMSND]^2 + [BC\text{-}RMSND]^2)\right]^{\frac{1}{2}} \quad (11)$$

Comb-RMSND was used to rank the candidate models by the best-fitting (or smallest deviation from) the reference constraints.

4 Results

We report the results of our structure model parameters searches compared to the geophysical, bulk compositional, and combined constraints. Section 4.1 presents the results of this analysis with geophysical constraints only, and Section 4.2 shows the effects of overlaying bulk chemistry and combined constraints. Our model database can be found at the University of Florida's Institutional Repository (IR@UF, http://ufdc.ufl.edu/ufir).

4.1 Geophysical

While the majority of sampled models did not yield satisfactory *zscores*, a portion of the sampled models achieved a geophysics *zscore* $\leq 2\sigma$. Figure 3a shows the results of model fitness to the observed mass and MOI for all models. For reference we note the mass and MOI *zscore* values for Weber et al. (2011), 632, and Garcia et al. (2011, 2012), 137, found by integrating their published density profiles. The distribution of models in mass and MOI space displays a long tail of models that over-predict mass (e.g., due to an overly large core) and under-predict MOI (i.e., due to excess mass within the outer layers). The appearance of clusters of models display the grid search sampling increment, with a dense cluster close to the origin largely composed of models from the DE search.

The influence of temperature is visible when the models are separated according to thermal profile (Figure 3b, CH-H shown). We note a positive ~50σ shift in mass deviation between the MaxT and MinT CH-H cases. Similar shifts were found for the CH-T and CS subclasses (see Figure S3).

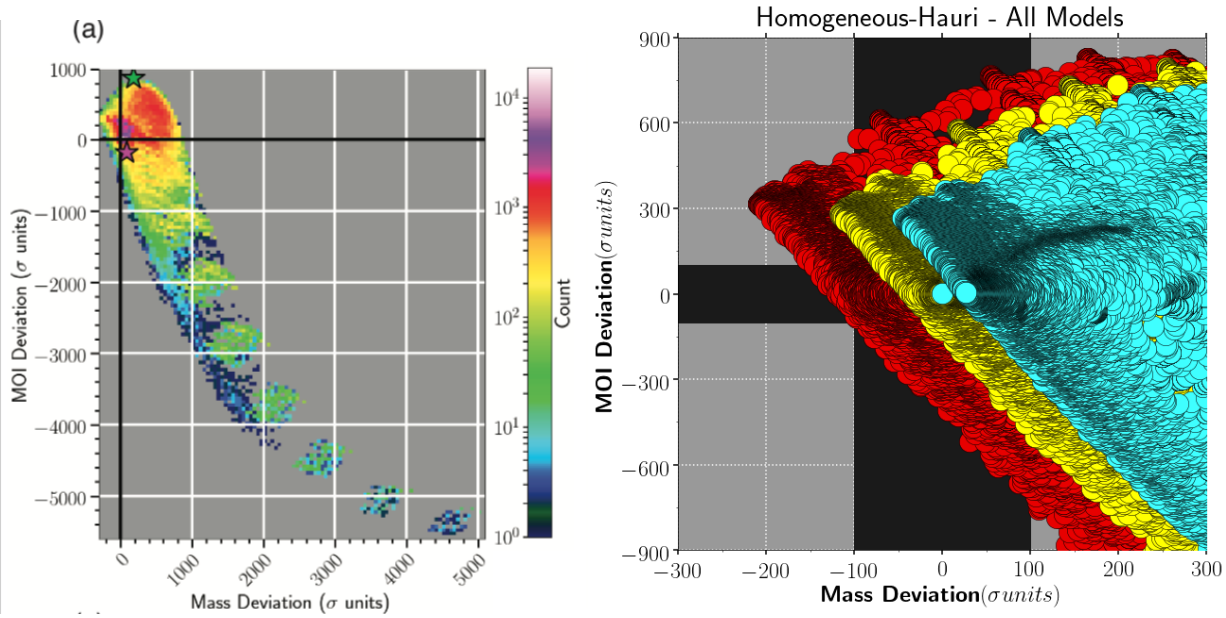

Figure 3. (**a, b**) The total model count distribution from all model subclasses (CH-H, CH-T, and CS), as a function of the number of standard deviation misfits from observational Mass and MOI. The map is color-coded according to the number of models that fall within each gridded cell with bin sizes of 50σ (**a**) (for 1σ zoom, see Figure S3). Overlaid are the calculated Mass and MOI deviations for the seismic/density models from Garcia et al. (2011, 2012) (pink star, *G-RMSND* of 137) and Weber et al. (2011) (green star, *G-RMSND* of 632). (**b**) The influence of temperature is shown for the three CH-H subclasses (red: MaxT, yellow: MeanT, cyan: MinT) within a zoomed window (for the full distribution of CH-H models, see Figure S3). This shows a systematic shift where decreased temperature corresponds to increased mass, and is due to material densification with decreasing temperature.

Figure 4 shows the variety of stratigraphic configurations within the lowest (≤2σ) Mass and MOI zscores. Low sigma models were found for all three CS selenotherms, however, within the CH classes, only the CH-H MaxT and MeanT and the CH-T MaxT achieved the same. The lowest *G-RMSND* values achieved for the CH-H MinT, CH-T MeanT, and CH-T MinT classes (those classes that did not have members that met the ≤2σ requirement) are 18, 32, and 81, respectively.

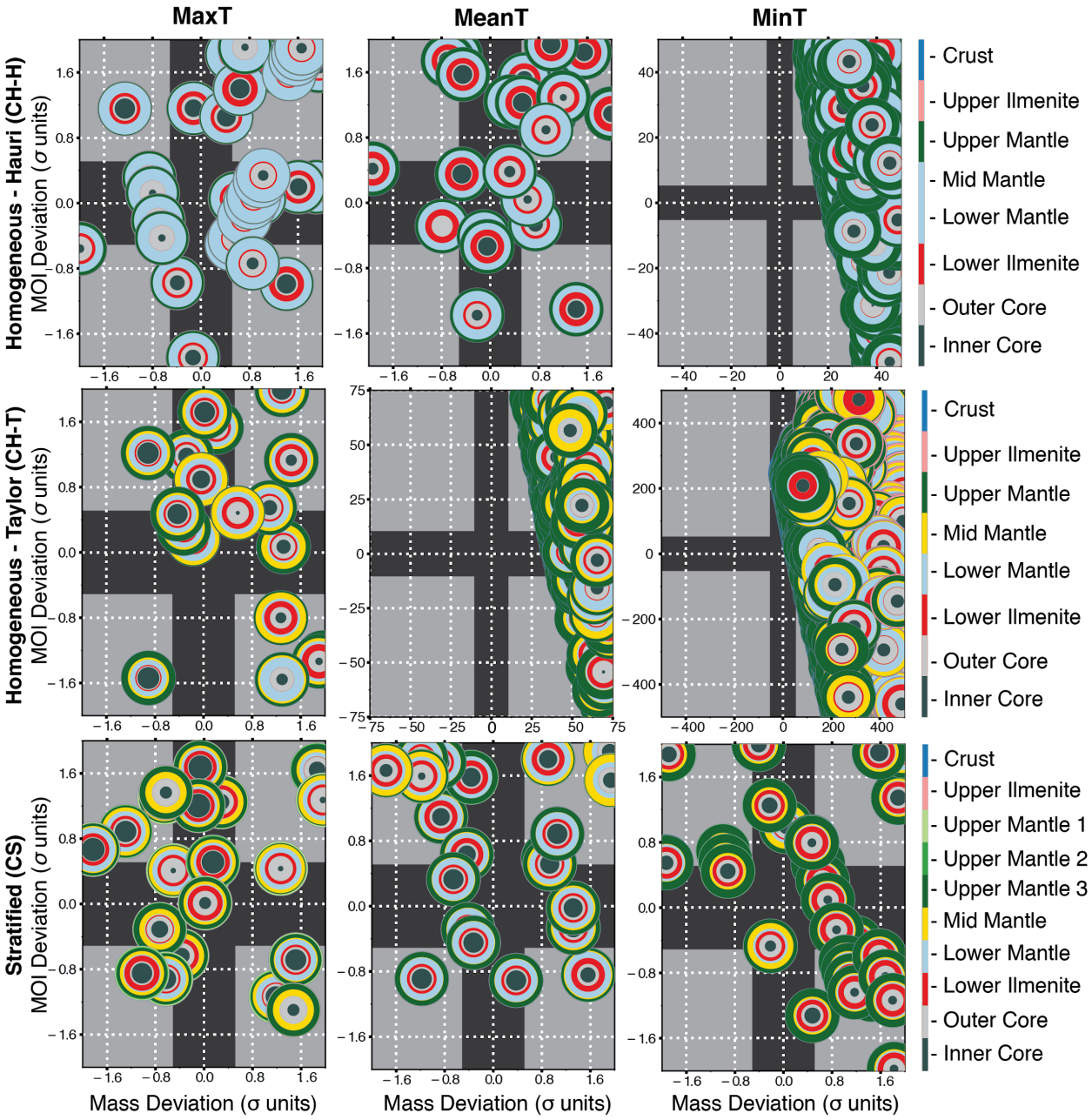

Figure 4. Low *zscore* geophysical results with respect to mass and MOI for all classes of model. The black bars highlight the region of lowest *zscore* values, ±2σ for all model subclasses except CH-H MinT, CH-T MeanT, and CH-T MinT, where the best-fit models are limited to ±50σ, 75σ, and 500σ windows, respectively. Color bar, right, indicates layer names. See Figure 1 for the mineralogy of each layer. Not that the axis scales vary for each panel.

The top 30 models for each of the three model classes, CH-H (S5a), CH-T (S5b), and CS (S5c), are shown in Figure S5 and are ordered from smallest to greatest *G-RMSND*. The bottom panels depict the structure of each lunar candidate model as a stratigraphic column. The top panels show the corresponding mass and MOI deviations, as well as *G-RMSND* values, for each stratigraphic column. The colored diamonds along the x-axis indicate each model's

corresponding thermal profile. Although the size of the inner and outer cores are variable, the sum, i.e., the total size of the core, is limited to a narrow range of thicknesses for all three model classes. Each of the top 30 models possess little-to-no upper ilmenite-bearing layer. However, we observe that most of the models contain a substantial lower ilmenite-bearing layer. All other layers have variable thicknesses. We note that all of the lunar candidate models featured in the top 30 list were generated by the differential evolution (DE) search and have *G-RMSND* values less than 2.5 (Figure S5), speaking to the strength of this technique.

For models with low *G-RMSND*, we observed distinct stratigraphic layer correlations (Figure 5). For models with low *G-RMSND* values, we observed a near 1:1 correspondent degeneracy between the inner and outer core sizes (Figure 5a) with a well-constrained total core thickness (Figure 5c). There is a small but non-zero upper ilmenite-bearing layer thickness visible across the full range of Total Core sizes with low *G-RMSND* (Figure 5b). The Lower Ilmenite thickness varies over a wide range from 0 - 500 km , however, the total volume of Ilmenite is narrowly defined, with a slight dependence on the total core size (Figure 5e). A decrease in Total Ilmenite volume corresponds to an increase in Total Core thickness. The thickness of the Total Mantle increases with increasing Total Core size (Figure 5d). Lastly, the upper ilmenite-bearing layer volume appears largely unaffected by changes in the lower ilmenite-bearing layer volume (Figure 5f). Similar trends as shown in Figure 5 are observed across all nine subclasses.

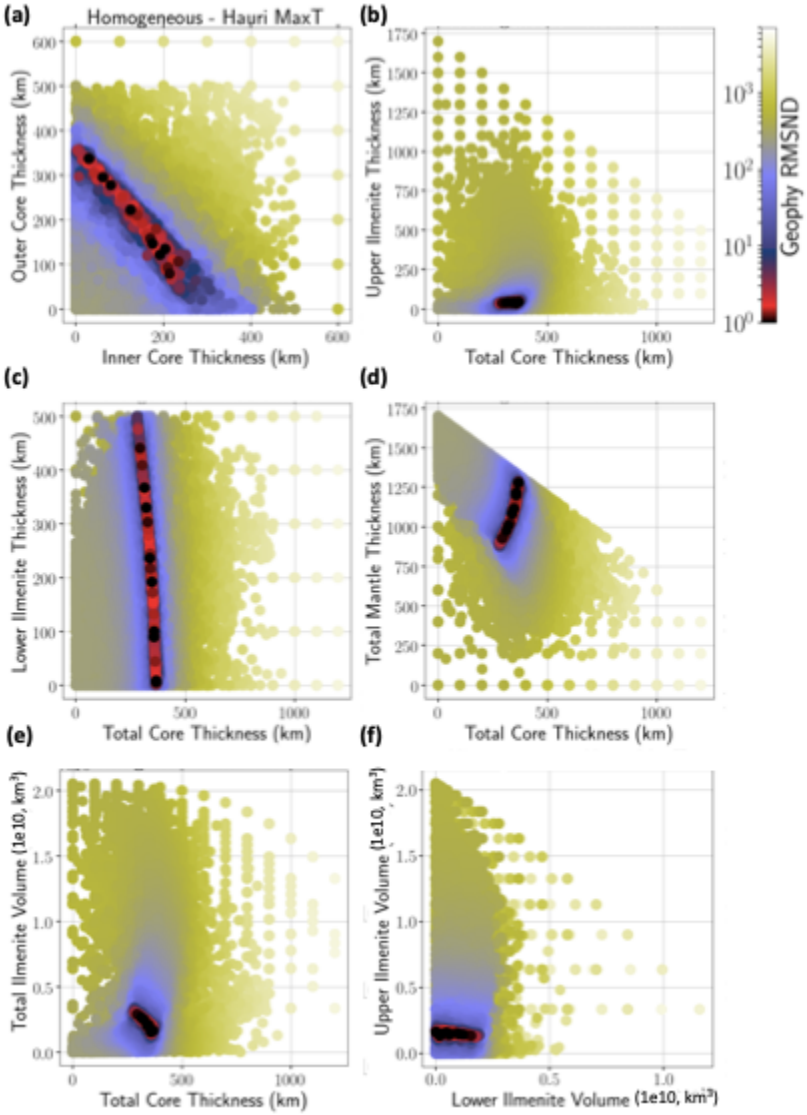

Figure 5. Structural trade-offs between stratigraphic layers (indicated in axes). Each circle represents a lunar candidate model color coded by *G-RMSND* (scale bar located to the right of panels). *Total Core* refers to the sum of the inner and outer core layers. *Total Mantle* refers to the sum of the upper, mid, and lower mantle layers. Note the exclusion of the upper and lower ilmenite-bearing layers within the *Total Mantle*. See the main text for details.

To more fully explore layer trends across all nine model subclasses, we compiled key model parameters onto box-and-whisker plots (Figure 6). The enhanced box-and-whisker plots each sampled lunar candidate model as a left-justified horizontal line where the length and color are scaled according to the model's RMSND value. Shorter lines and hotter colors correspond to smaller values. Smaller values are plotted on top of larger ones. To the left of each column of scaled lines are black and white boxes indicating that all components within the model RMSND value are less than or equal to 1σ and 3σ (1 or 3 zscores) misfit, respectively. A red arrow tail

points to the location of the lowest RMSND value of the subclass. The minimum and maximum range of sampled models is indicated by the whisker shown by upper and lower red triangles connected by a black dotted line. The standard box-and-whisker show a green box models within zscore<3 and a black box for values less than zscore < 1 with the red horizontal line indicating location of best-fit model within the subclass.

We observe, across all model classes, the best-fit models (shortest lines, hottest colors) appear in a narrow-ranged cluster on top of models with larger RMSND values (longer lines, cooler colors). In Figure 6b, the largest RMSND values are all located at large Total Core sizes, and are separated from smaller values. The red arrow tails show a trend toward smaller Total Core size with decreasing thermal profile in the CS model classes. We also see in Figure 6b no low sigma candidate models were found with zscore < 3 for the CH-H Max, CH-H MinT, CH-T MeanT, and CH-T MinT model subclasses.

The *Total Core* size as a function of *BC-RMSND* value ranges from 0 - ~900 km thick for models where all oxide deviations have $zscore \leq 3$ (Figure S4a, middle panel). The largest *BC-RMSND* values are distributed throughout the full range of sampled *Total Core* thicknesses. For the *Comb-RMSND* (Figure S4a, bottom panel), the distribution pattern of *RMSND* values largely resembles what was found for the *G-RMSND* values, where the largest values are only associated with large *Total Core* size. The red arrow tail that points to the location of the best-fit models spans a narrow range of *Total Core* sizes across all nine subclasses (see Table S5 for summary).

For layers plotted as a function of *BC-RMSND*, all nine model subclasses produced lunar candidate models that fall within 3σ, but only the CH-T model class has models that fall within 1σ (for all three thermal profiles) (Figure S4). For layers plotted as a function of *Comb-RMSND*, the CS model class produced candidate models that have *zscore* values for all constraints ($zscore_{all}$) that fall within 3σ for all three thermal profiles. For the CH-T model class, only the MaxT thermal profile produced models that fall within $zscore_{all} \leq 3$, similar to what was found with *G-RMSND*, but unlike *BC-RMSND*, all three thermal profiles fall within $zscore \leq 3$. For the CH-H model class, only the MeanT thermal profile produced candidate models with $zscore_{all} \leq 3$, which is a departure from both the *G-RMSND* and *BC-RMSND* cases. The CH-H-MaxT, CH-H-MinT, CH-T-MeanT, and CH-T-MinT model subclasses did not contain any candidate models with $zscore_{all} \leq 3$.

The Upper Ilmenite volume as a function of *BC-RMSND* value (Figure S4b, middle) has a distribution that tapers towards 0 km^3: there is a steady decrease of *RMSND* value with

decrease in Upper Ilmenite volume. Low *BC-RMSND* valued models are not co-located with larger valued models. This pattern was observed for all nine model subclasses, and was not observed for any other stratigraphic layer (or combination of layers) or *RMSND* type. Models where all oxide deviations have *zscore* ≤ 3, range from 0 to 0.2e10 km^3, and the best-fit models are at or near 0 km^3. For the *Comb-RMSND* (Figure S4b, bottom), the largest *RMSND* values are distributed across the full range of sampled volumes. In all nine subclasses there is little to no Upper Ilmenite volume, with the exception of CH-H-MeanT, CH-T-MaxT, and all three CS, do contain a small volume of Upper Ilmenite in the best fit models.

Slightly larger ranges were observed for the lower ilmenite-bearing layer volume (Figure S4c). For all nine subclasses, there is little-to-no Lower Ilmenite volume for low *BC-RMSND* values (Figure S4c, middle). The large G-*RMSND* values are distributed across the full range of sampled volumes, which differs from the Upper Ilmenite volume which taper towards the best-fitting point. The *Comb-RMSND* (Figure S4c, bottom) follows a similar pattern to that found for the *G-RMSND* values. The Total Ilmenite volume is also considered in Figure S4d with similar conclusions to the Upper Ilmenite.

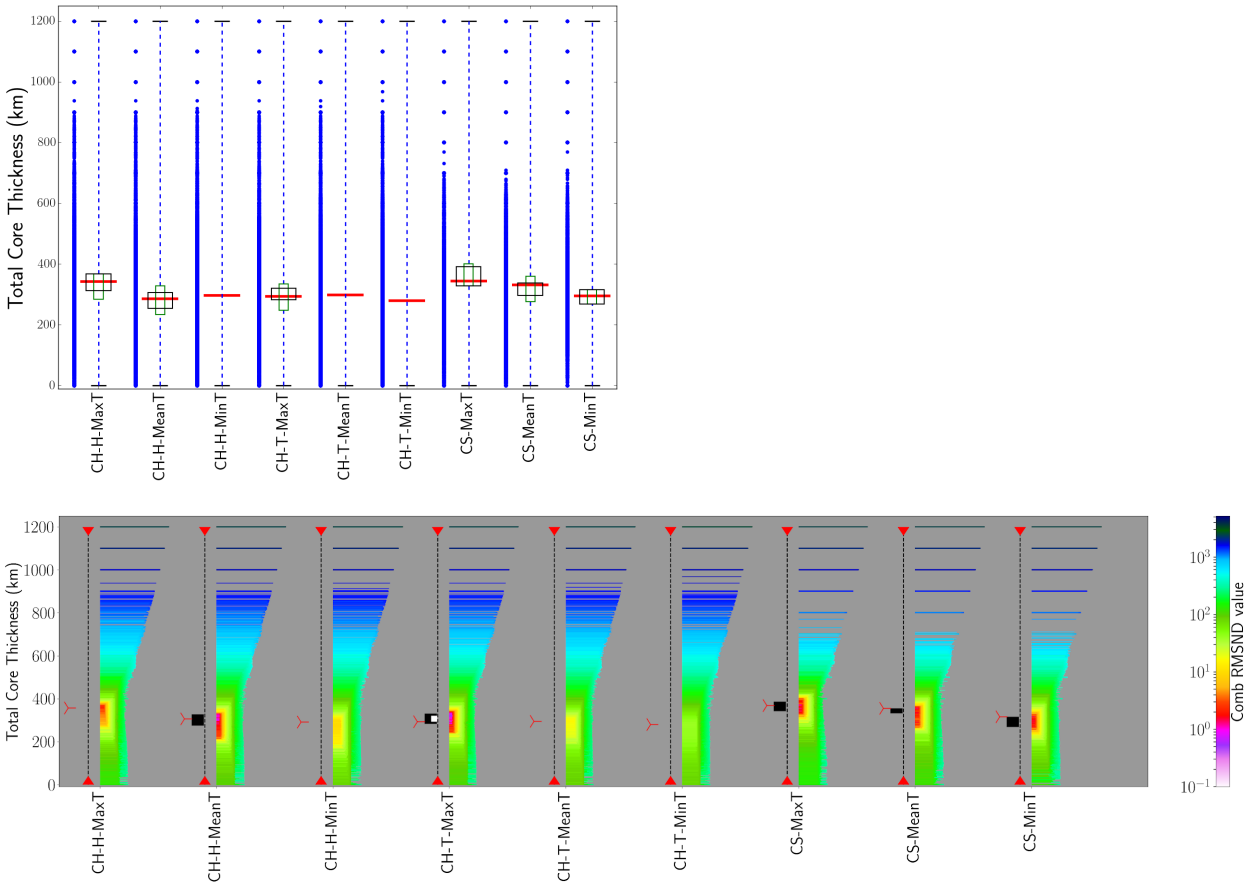

Figure 6. Box-and-whisker plots of the Total Core thickness for all model subclasses as labeled on x-axis. Each sampled lunar candidate model plots as a left-justified line where the length and color vary according to the model's Comb-RMSND. High RMSND values correspond to the longer horizontal lines, and low RMSND values to short lines. Low RMSND values are plotted on top of larger values. To the left of each column of scaled lines are the "simplified" ranges where the min/max sampled layer thickness (or volume) is shown by red triangles and connected by a black dotted line. The black and white boxes indicate that all components within the RMSND value are less than or equal to 1σ and 3σ (1 or 3 zscores) misfit, respectively. The best fit thickness (or volume) is marked with a red arrow tail for each model subclass. For additional Box and Whisker plots, see Figure S4.

Seismic observations have the potential to also place a strong constraint on the internal structure of the Moon. In order for seismic velocity profiles to be used as robust constraints on the internal structure of the Moon, they should be sensitive to the mineralogy and thermal condition across depths in the lunar interior. We tested the sensitivity of seismic velocity profiles to the thermal state and mineralogy as follows. In Figure 7 we compare the seismic and density profiles of the lowest G-RMSND (best-fit) lunar candidate model for each of the CH-H, CH-T, and CS model classes from Figure S5 to those derived directly from the Apollo seismic analyses of Garcia et al. (2011, 2012) and Weber et al. (2011). The top panels show the profiles from the

best-fit model, as well as two counterpart models with the same layer configuration but different thermal profiles, and the structures from Weber et al. (2011) and Garcia et al. (2011). The bottom row plots the difference between the best-fit and thermal counterpart models Vp, Vs, and density. We note that the *G-RMSND* < 1 for each of the best-fit models, but the zscore misfit of the temperature companion models range between 60 - 130 (large misfit). Nevertheless, only very minor differences were observed between the seismic and density profiles of the well-fit models, their thermal counterparts, and the Weber et al. (2011) and Garcia et al. (2011, 2012) profiles. Both the best-fit models and their thermal counterparts generally reproduced the observed velocity and density structures with the exception of the crust and lower mantle/core, which indicates that seismic profiles alone cannot be used as robust constraints of mineralogy and thermal structure in the lunar interior, thus emphasizing the need to use physical quantities such as mass and MOI as additional constraints

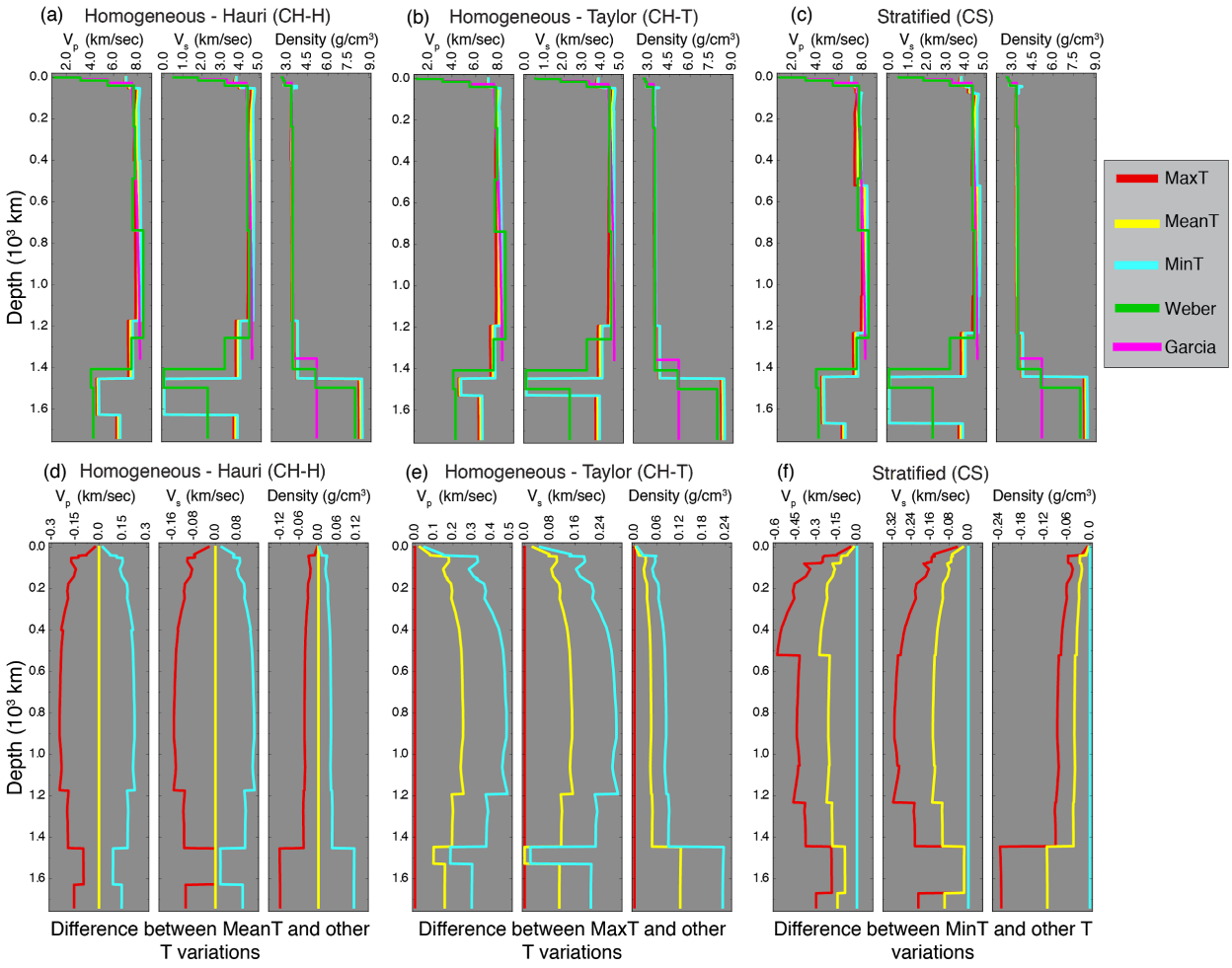

Figure 7. Comparison of a well-fit model (low *G-RMSND*) and the corresponding thermal counterpart models (same layer configuration, different thermal profile) from the CH-H (a,d), CH-T (b,e), and CS (c,f) model classes. Panels (a,b,c) show seismic velocities V_p, V_s, and density profiles for each of the well-fit models along with their counterparts, and are compared to the Garcia et al., (2011, 2012) and Weber et al., (2011) models. Panels (d,e,f) show the difference between the well-fit models (the model with a constant value of zero in each panel) and their counterparts. The *G-RMSND* values for the well-fit models are; CH-H: 0.5 (MeanT), CH-T: 0.2 (MaxT), and CS: 0.5 (MinT), while all corresponding counterparts are > 80. *G-RMSND* values for Garcia et al. (2011, 2012) and Weber et al. (2011) are 137 and 632, respectively. Apparently, the large range in thermal profiles do not translate into large variations in seismic velocity, and model fit to Mass and MOI are not indicators of fit to estimates of seismic velocity.

4.2 Bulk Composition and Combined RMSND

For each of the sampled lunar candidate models generated by the search methods, we calculated the misfit to bulk chemistry, both as *zscore* of each oxide's deviation (equation 8) and as *BC-RMSND* values (equation 10). We observed that the minimum *G-RMSND* value per *BC-RMSND* value follows a curve such that the minimum *G-RMSND* decreases with decreasing *BC-RMSND* value (Figure S6). The lowest *G-RMSND* values only correspond to low *BC-RMSND*

values. Equivalent distributions were observed for the CH-H and CH-T model classes (ref supplemental figures). Figure 8 shows the top 30 models that have $zscore_{Mass}$, $zscore_{MOI} \leq 2$, then organized from least to greatest *Comb-RMSND* values for CH-H (a), CH-T (b), and CS (c) model classes. Similar to the construction of Figure S5, the bottom panels depict the structure of each lunar candidate model as a stratigraphic column. The middle panels show the corresponding Mass and MOI deviations, and the *G-RMSND* values. Added here, are the *BC-RMSND* and *Comb-RMSND* values. The top panels show oxide deviations from the mean reference bulk composition in terms of their *zscore*. As was found in *G-RMSND*-only case (Figure S5), for all three model classes the inner and outer core thicknesses are variable, but the *Total Core* size is limited to a narrow range of thickness. Likewise, all the models shown possess little to no upper ilmenite-bearing layer, but a variety of thicknesses were observed for all other layers. In general, *RMSND*≤3 for all the model classes within the top 30.

In terms of bulk chemistry, the CH-H models show a rapid increase in *BC-RMSND* corresponding to a rapid increase in TiO_2 *zscore* from ~1.5 - 6, which is a component of the ilmenite-bearing layer. A vivid example of its effect can be seen in the top CH-Hmodels, where TiO_2 *zscore* clearly increases with Lower Ilmenite thickness and/or Upper Ilmenite thickness, implying a limitation of Total Ilmenite volume from the bulk chemistry constraints. Since the comparison between the volumes of upper and lower ilmenite-bearing layer is difficult from the layer thicknesses in Figure 8, we refer to Figures S4 for details of the Total Ilmenite volume.The *zscores* were lower than those of TiO_2 for the other five oxides. For most of the top 30 models shown, *BC-RMSND* was the primary contributor to increases in CH-H *Comb-RMSND* values, and only models from the MaxT and MeanT thermal profiles are featured.

Of the three model classes, the CH-T models display the best fits to bulk chemistry, as well as showing a steady increase in *G-RMSND*. Only models from the MaxT thermal profile are featured in the top 30 models. A near constant depletion of Al_2O_3 of ~-0.8 was observed across all the top 30 models. Misfit of TiO_2 was variable, but ranged between ~-1.0 - 2.4. Very little misfit was observed for the remaining four oxides. For most of the top 30 models shown, the *G-RMSND* was the primary contributor to the increases in CH-T *Comb-RMSND*.

Of the three model classes, the CS models display the greatest variety of individual oxides with large misfit, but most models are depleted in Al_2O_3 (~-2.0) and enriched in SiO_2 and TiO_2 (~1.0 - 4.5). All three thermal profiles appear in the top 30 list for CS models. With some exceptions, the *BC-RMSND* was the primary contributor to increases in *Comb-RMSND* values for most of the models.

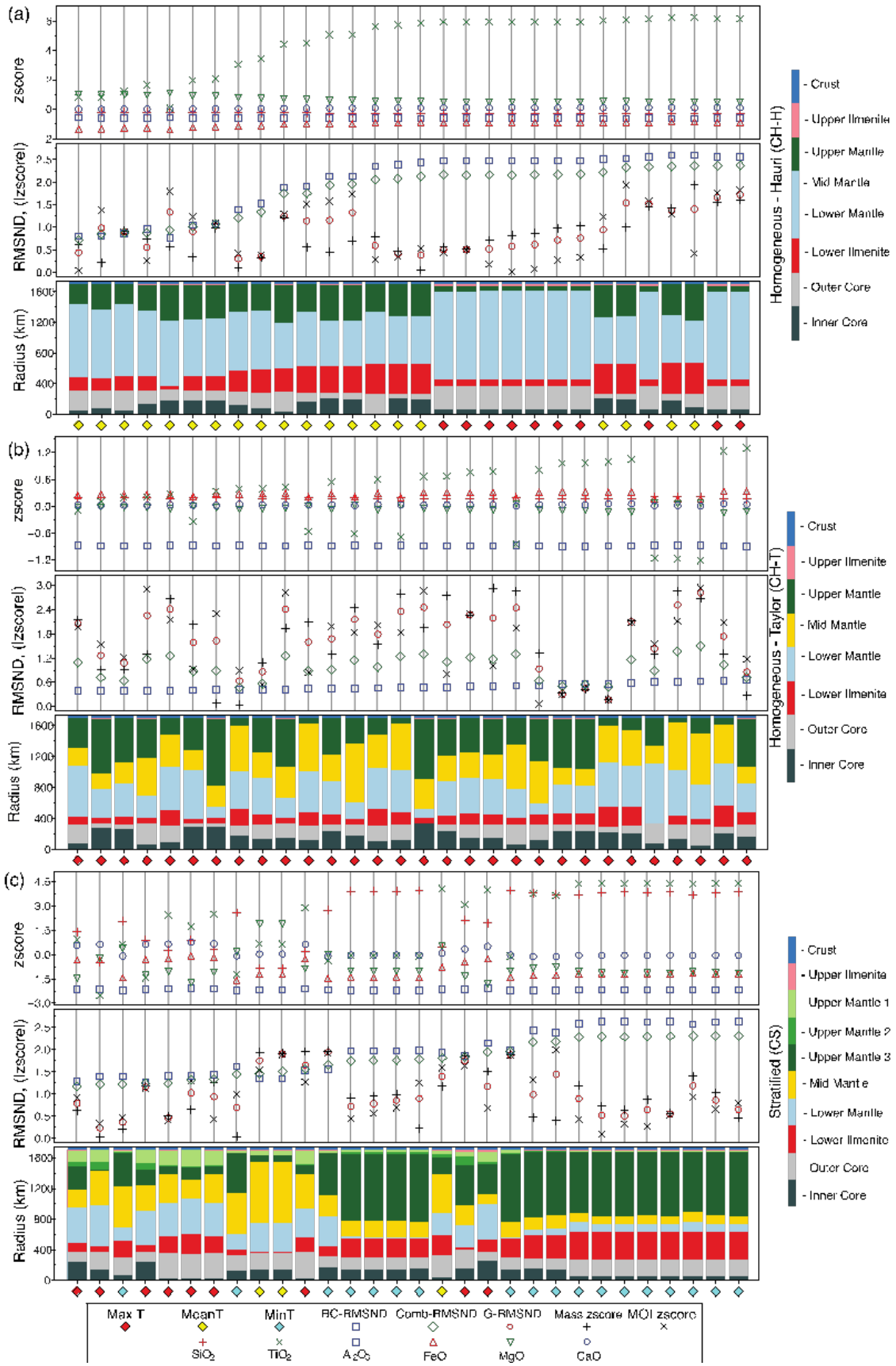

Figure 8. (caption continued on next page)

Figure 8. The top thirty best-fit model candidates for (a) CH-H, (b) CH-T, and (c) CS model classes are compared in terms of oxide deviation (top panel); deviations for Mass, MOI, and *RMSND* (middle panel); and model stratigraphic structure with color coded layers (bottom panel). The stratigraphic legend is to the right of each set of panels. Diamonds along the x-axis indicate model temperature profile. Models are ordered by lowest *Comb-RMSND*. For compositional description of each layer, see Figure 1.

Table S5 summarizes the range of layer thicknesses and volumes that have $zscore \leq 2$ for all components within *G-RMSND* and *BC-RMSND*, and $zscore \leq 3$ for all components within *Comb-RMSND* for all model subclasses. Comparing our final ranges of thickness to our originally sampled ranges (as listed in Table 1) indicates how well our routine has constrained thickness estimates, and quantifies the relative effectiveness between *RMSND* constraints. Model counts by subclass are provided in the supplement text S2. Note that the Upper Ilmenite range has artificially low reduced ranges, as it was tested to the full lunar radius (minus the crust).

For *G-RMSND* best-fit models, we constrain the total core to within 234 - 401 km thick regardless of thermal profile or model class. This represents a total core that is 14% of the initial sampled range. However, large variability exists in outer and inner core thicknesses, where both layers range from 0 - ~330 km. The volumes of lower, upper, and total ilmenite-bearing layers all show substantial reduction from their initial ranges (due to radial geometry, the lower ilmenite-bearing layer thickness did not reduce much based-on *G-RMSND*, although the upper ilmenite-bearing layer thickness did.). Of these three, Lower Ilmenite and Total Ilmenite volumes reduced to ~13% of their initial sampled extents. While the lower bound of the upper and lower ilmenite-bearing layer volumes is zero, the Total Ilmenite volume lower bound is non-zero for *G-RMSND*. A total of 141 lunar candidate models were included for the *G-RMSND* final ranges.

For the *BC-RMSND*, reduced normalized range for the Total Core size was much greater than that based on the *G-RMSND*. The final range of the upper ilmenite-bearing layer thickness is thin (0-25 km), and there was nearly no reduction in range of the Lower Ilmenite thickness. However, the volumes of Lower, Upper, and Total ilmenite all have reduced normalized ranges that are less than half of the geophysical based ranges. We observed that the Total Ilmenite volume lower bound is non-zero, and higher than in *G-RMSND*. More than 38,000 lunar candidate models were included for the *BC-RMSND* final ranges.

When the results from the previous two are combined, we observed improved constraints on layer thicknesses and volumes. The range of Upper Ilmenite thickness was similar to that

found with *BC-RMSND* alone. However, when considering the combined constraints, the *Total Core* thickness was constrained to be within 269-387 km, narrower than *G-RMSND* or *BC-RMSND* alone. With the *Comb-RMSND*, the reduced normalized ranges of total mantle thickness was 15%, as compared to *G-RMSND* (25%) and *BC-RMSND* (53%). The range of Total Ilmenite volume falls between *G-RMSND* and *BC-RMSND*, also with a non-zero lower limit. A total of 100 lunar candidate models were included for the *Comb-RMSND* final ranges.

5 Discussion

5.1 Constraints on mantle stratification and present-day selenotherm

The present-day Moon is likely in-between a perfectly stratified and completely homogenized state. If the present-day Moon is more homogenized, our models favor warmer selenotherms, with a temperature profile closer to our MeanT or MaxT profiles. Such selenotherms are consistent with the hotter CMB temperature proposed by two recent experimental studies (Mallik et al., 2019; Zhang et al., 2019). A colder Moon (following the Min T profile and similar to that predicted by the recent study by Kawamura et al., 2017) is only allowed in our models if the present-day Moon retained most of the stratigraphy from LMO crystallization and has not undergone homogenization since due to mantle mixing and dynamics.

5.2 Comparison to seismic profiles

Our models do not attempt to capture the details of the crustal structure of the Moon, including regolith, mega-regolith, and additional layering; rather we imposed a uniform 40 km thick anorthitic crust. We also assumed that our initial compositional models (Figure 1) represented the laterally averaged compositional structure. Yet despite the minimalist design of our compositional models, our results are seen to generally match to the Weber et al. (2011) and Garcia et al. (2011, 2012) profiles for all three model classes. Figure 7 demonstrates the shifts in seismic and density profiles that occur with changes in thermal profile, which is not a surprising result. However, the relative changes are on the order of ~3% difference in seismic velocity, and <2% difference in density, which are both potentially within the measurement error of the Apollo seismic data. Recall that, in each of the model classes, two of the three lunar candidate model profiles shown in Figure 7 have *G-RMSND* values >60, and indeed the Weber et al. (2011) and Garcia et al. (2011, 2012) profiles have even higher *G-RMSND* values (632 and 137, respectively). Therefore, the current constraints on seismic velocity are insufficient to constrain the density and compositional structure of the lunar interior without applying additional constraints.

5.3 Combining Geophysics with Bulk Composition

While we cannot rule out either a stratified or homogeneous mantle, bulk chemistry clarifies the trends in layer thickness for a given temperature profile and puts firm limits on some layers. Some curious features appear when layer thicknesses of the *BC-RMSND* are displayed versus one another (Figure 5). Lower ilmenite-bearing layer volume, rather than appearing independent from upper ilmenite-bearing layer volume, now trades off as per the limitation on the total Ti content of the Moon. As is shown by the linear trade-off in Upper and Lower Ilmenite volumes in Figure S7a, the total volume of the ilmenite-bearing layer (upper and lower combined) is a near constant and is controlled by the Ti concentration of the bulk Moon. To this effect, the total mantle thickness increases with core growth within the geophysical constraints. However, within the chemistry the best fit region is much wider for total mantle thickness versus total core (Figure S7b). The Upper and Lower Ilmenite volumes are also well constrained. Bulk chemistry limits ilmenite-bearing material and therefore sometimes temperature profile (Figure S4). As the deviation of Ti goes up, it drives an increase in *BC-RMSND*. For instance, in CH-H-MaxT, the best-fitting lower ilmenite-bearing layer thickness seems to vanish with the bulk chemistry implementation. This also occurs in the Taylor model class, but for Al content in the crust. A noteworthy feature from the bulk chemistry in the CS model class is that not only Ti but also Si is limited. This is because our CS mantle is based on the model from Snyder et al. (1992), which features a pure orthopyroxene layer rich in Si relative to olivine. This layer can be seen in the stratigraphic column plots of Figure 8.

An interesting observation in the top 30 models in Figure 8 is that, irrespective of model class, every best-fit model has a prominently thick lower ilmenite-bearing layer which supports the idea that a mantle overturn process involving sinking of the upper ilmenite-bearing layer through the mantle took place at some point in lunar history. Also, it is noteworthy that each of the top 30 models contain a finite volume of upper ilmenite-bearing layer, which is likely a residue from the mantle overturn process. These upper and lower ilmenite-bearing layers not only redistribute heat producing elements within the Moon (which has implications for the dynamics of the lunar interior), but the presence of a residual upper ilmenite layer may have implications for potential assimilation of these Fe-Ti rich cumulates with a Mg-rich primary partial melt to produce the chemistry of certain lunar basalts (e.g. Mallik et al., 2019).

5.4 The lunar core

Our models determine tight range of possible *Total Core* sizes of **269 - 387 km** (Figure 6, 8 and Table S5), consistent with previous results (Hood et al., 1999; Shimizu et al., 2013,Garcia

et al., 2011, 2012; Weber et al., 2011;Yan et al., 2015). *BC-RMSND* applied no direct constraints to the *Total Core* size, which is sensible since the bulk chemistry constraints only described the silicate mantle. We cannot independently constrain inner and outer core thicknesses, as the densities of liquid and solid iron are similar.

In our model, for simplicity, we assumed that the lunar core was pure iron and not allowed for the existence of any light elements in the core. The light element composition of any possible fluid outer core is debated, with different studies favoring sulfur (Jing et al., 2014), carbon (Steenstra et al., 2016). The addition of light elements would lower the core's density, reducing the mass and MOI of the Moon for a fixed core size. The effect of light elements on global mass and MOI likely trades off with the mass of other layers, in particular the lower and upper ilmenite-bearing layers. Using both geochemical and geophysical constraints on the light element composition of the lunar core should be considered by future work.

5.5 Upper and Lower Ilmenite-bearing Layers

Across all nine model subclasses, we observed little-to-no upper ilmenite-bearing layer. This was consistent for both the geophysical and bulk compositional *RMSNDs*, but was especially robust from *BC-RMSND*, where small values coincide with a small volume of ilmenite-bearing material (Figure S4b, middle). Similarly, we observed little-to-no Lower Ilmenite volume (Figure S4c), but Total Ilmenite is non-zero (Figure S4d). Figure S7 demonstrated that a trade-off exists between the upper and lower ilmenite-bearing layers. For the case of a zero Upper Ilmenite layer, a non-zero volume of lower ilmenite-bearing material at the CMB exists. Bulk compositional constraints limit the total amount of TiO_2 (and therefore ilmenite) in the silicate mantle. For many candidate models, deviations in TiO_2 are due to enrichment, especially for models with a non-zero volume of upper ilmenite-bearing material (Figure 8). Furthermore, the constraints on MOI limit the volume of the upper-ilmenite material, where large volumes are penalized for adding excessive mass to the outer radii of the lunar interior. Therefore, our models do not discount the possibility that any substantial ilmenite-bearing layer that formed during LMO crystallization may have subsequently been transported to the CMB or mixed with the rest of the mantle.

5.6 Limitations of this Study and Future Directions

In our stratified mantle models, we assumed that the stratification was introduced by the crystallization of a whole-mantle MO. However. the depth of the lunar MO is uncertain. Current estimates state a MO of around 700 km thick, based on the thickness of the crust as obtained from GRAIL results (Elkins-Tanton et al., 2011). If the Moon only had a partial-mantle MO

there would be a substantial primitive lower mantle in the Moon, which has not been considered in this study. However, the methods outlined here are applicable to other models that do consider a partial MO, such as Charlier et al. (2018) and Lin et al. (2018a,b).

Our reference bulk composition is derived from a compilation of available compositional models, but these models largely consist of Taylor-like compositions, which bias our geochemical constraints towards a Taylor-like lunar structure. For example, in Figure 4S the best-fit models found for the CH-T model class feature the lowest *BC-RMSND* values across all models. To help correct this, a weighting could be applied when averaging the available compositions. However, we elected not to do this because the validity of one composition relative to another is uncertain. The available bulk compositional models assume that estimates based on Apollo samples and remote spectroscopy of the lunar surface represent the bulk silicate mantle and crust. This may not be the case, and future sample return missions are likely needed for improvements in this area. The imposed bulk chemistry reference can be tweaked for future work to re-evaluate the ensemble of best-fitting models.

This study does not take the hemispheric dichotomy of the Moon into consideration. Given that heat producing elements are more concentrated on the surface of the near side rather than the far side, it is not surprising if the near side follows a hotter selenotherm than the far side, and the hemispheres have had distinct evolutionary histories. Future seismic analyses from a global lunar geophysical network may shed light into the hemispheric dichotomy and resolve the potentially distinct interior structures of each hemisphere.

Though not treated in this study, an additional constraint on lunar structure could be provided by the observed tidal dissipation quantified by the Love numbers k2 and h2. However, tidal dissipation depends on both mantle temperature and mineral grain size (Faul & Jackson, 2005; Nimmo et al., 2012). Grain size is not well constrained within the lunar mantle, and so this.

Lastly, we performed two preliminary studies to investigate and motivate the sinking mechanisms for ilmenite-bearing layer through the mantle. These are summarized briefly here and the reader is directed to Text S1 for full description. We examined whether the ilmenite-bearing layer proposed to have formed below the anorthite crust after 95% MO crystallization can sink, either as a liquid or a solid, and constitute the proposed melt layer within the lunar lower mantle. As a liquid, we found that Fe+Ti-rich partial melt must reach a density crossover point of ~180 *km*, with limited mantle assimilation, to become negatively buoyant with respect to the surrounding mantle. This crossover depth increases with increasing amounts of mantle

assimilation. We considered impacts as a possible mechanism to transport ilmenite to depth, and found that it is unlikely that impacts are capable of transporting significant amounts of Fe-Ti-rich partial melt beyond the crossover depth. As a solid, we performed mantle convection modeling and demonstrated that an ilmenite-bearing layer can sink and persist at the CMB as a solid for a homogeneous mantle. Further convection modeling is required to more fully capture the ilmenite-bearing layer overturn scenario in a stratified model composition.

6 Conclusions

We have explored the range of possible lunar interior structure models by combining geophysical and geochemical constraints. To do this, we developed a computational tool called *Selenoman* to calculate the physical properties of the lunar interior and compare against observations of mass, MOI, and bulk chemistry. We tested 383,234 different 1D lunar candidate models across nine combinations of compositional classes and temperature profiles. We found that mass and MOI alone narrowed the scope of likely composition and selenotherm combinations, but the addition of bulk compositional constraints further constrained the range of plausible structures. Our inherently multidisciplinary approach is applicable to any planetary body where estimates of bulk chemistry and total mass and moment of inertia are available, such as Mars.

We found both compositionally homogenous and compositionally stratified lunar candidate models that match the observational constraints applied in this study but find that imposed temperature gradient qualifies the likelihood of our proposed profiles. Within our best-fit models we observed a *Total Core* size (sum of inner and outer core size) to be consistent with previous observations.

Our lunar candidate models are consistent with an ilmenite-bearing layer at the CMB in the present-day Moon. The volume of a lower ilmenite-bearing layer was not well constrained, with acceptable models varying from 0-7.7e8 km^3. The resulting range of the upper ilmenite-bearing layer thickness was less than 24 km. Our best-fit models exhibited a non-zero volume of Total Ilmenite (sum of upper and lower ilmenite-bearing layers), and we found that the Upper and Lower Ilmenite volumes trade off to meet the total titanium constraint of the Moon. The use of bulk chemistry constraints reduced the range of ilmenite-bearing layer thicknesses found for observationally consistent models by introducing additional limitations on our results.

Despite the simplistic assumptions of our laterally averaged compositional structure, our results generally match the seismic and density profiles of *Weber et al.* [2011] and *Garcia et al.*

[2011, 2012] for all three model classes. We demonstrate that the shifts in seismic and density that occur with the change in temperature profile are potentially less than the measurement error of the Apollo seismic data. We conclude that current estimates of seismic velocities alone are insufficient to constrain the density and compositional structure of the lunar interior without applying additional constraints.

Acknowledgments

The lunar equations of state analysis algorithm developed for this project can be accessed at https://github.com/geodynamics/burnman. In addition, the compositional model database supporting this analysis can be found at the University of Florida's Institutional Repository (IR@UF), http://ufdc.ufl.edu/ufir.

This study originated as a group project at the 2014 CIDER summer program and our team would like to gratefully acknowledge the CIDER organization for their financial support through NSF grant number EAR-1135452 CIDER-II. The work also received support from the Alexander von Humboldt postdoctoral fellowship to AM, from NASA Headquarters under the NASA Earth and Space Science Fellowship Program - Grant "NNX14AP19H S02" to HFH, and NSF EAR 09-55647 to WRP. SJL gratefully acknowledges funding from NASA grant NNX13AO67H, NSF grants EAR-1947614 and EAR-1725349 and support from Harvard University's Earth and Planetary Sciences Department and Caltech's Division of Geological and Planetary Sciences.

The authors would also like to acknowledge helpful discussions with Anat Shahar, Wendy Panero, Hugo Jiménez-Pérez, Ulrich Faul, Phillippe Lognonné, Gordana Garapic, Ian Rose, Sanne Cottaar, Bob Myhill, Juliane Dannberg, Rene Gassmoeller, Bill McDonough, Lindy Elkins-Tanton, Anne Pommier, Len Srnka, Mark Panning, Quentin Williams, and Nicholas Schmerr that contributed to this work.

References

Le Bars, M., Wieczorek, M. A., Karatekin, Ö., Cébron, D., & Laneuville, M. (2011). An impact-driven dynamo for the early Moon. *Nature*, *479*(7372), 215–218. https://doi.org/10.1038/nature10565

Borg, L. E., Connelly, J. N., Boyet, M., & Carlson, R. W. (2011). Chronological evidence that the Moon is either young or did not have a global magma ocean. *Nature*, *477*(7362), 70–72. https://doi.org/10.1038/nature10328

Boukaré, C. E., Parmentier, E. M., & Parman, S. W. (2018). Timing of mantle overturn during magma ocean solidification. *Earth and Planetary Science Letters*, *491*, 216–225. https://doi.org/https://doi.org/10.1016/j.epsl.2018.03.037

Brown, S. M., & Grove, T. L. (2015). Origin of the Apollo 14, 15, and 17 yellow ultramafic glasses by mixing of deep cumulate remelts. *Geochimica et Cosmochimica Acta*, *171*, 201–215. https://doi.org/10.1016/j.gca.2015.09.001

Buck, W. R., & Toksoz, M. N. (1980). The bulk composition of the Moon based on geophysical constraints. In *Lunar and Planetary Science Conference Proceedings* (Vol. 3, pp. 2043–2058). Houston, TX.

Charlier, B., Grove, T. L., Namur, O., & Holtz, F. (2018). Crystallization of the lunar magma ocean and the primordial mantle-crust differentiation of the Moon. *Geochimica et Cosmochimica Acta*, *234*, 50–69. https://doi.org/https://doi.org/10.1016/j.gca.2018.05.006

Circone, S., & Agee, C. B. (1996). Compressibility of molten high-Ti mare glass: Evidence for crystal-liquid density inversions in the lunar mantle. *Geochimica et Cosmochimica Acta*, *60*(14), 2709–2720. https://doi.org/10.1016/0016-7037(96)00117-2

Cottaar, S., Heister, T., Rose, I., & Unterborn, C. (2014). Burman - A Lower Mantle Mineral Physics Toolkit. *Geochemistry, Geophysics, Geosystems*, *15.4*, 1164–1179.

Cottaar, S., Heister, T., Myhill, R., Rose, I., & Unterborn, C. (2016, April). BurnMan v0.9.0. *Zenodo*. https://doi.org/10.5281/ZENODO.546210

Ćuk, M., & Stewart, S. T. (2012). Making the Moon from a fast-spinning Earth: a giant impact followed by resonant despinning. *Science (New York, N.Y.)*, *338*(6110), 1047–52. https://doi.org/10.1126/science.1225542

Ćuk, M., Hamilton, D. P., Lock, S. J., & Stewart, S. T. (2016). Tidal evolution of the Moon from a high-obliquity, high-angular-momentum Earth. *Nature*, *539*(7629), 402–406. https://doi.org/10.1038/nature19846

Delano, J. W. (1980). Chemistry and liquidus phase relations of Apollo 15 red glass Implications for the deep lunar interior. *In: Lunar and Planetary Science Conference*, *1*, 251–288.

Delano, J. W. (1986). Pristine lunar glasses: Criteria, data, and implications. *Journal of Geophysical Research*, *91*(B4), 201. https://doi.org/10.1029/JB091iB04p0D201

Delano, J. W., & Lindsley, D. H. (1983). Mare glasses from Apollo 17: Constraints on the Moon's bulk composition. *Journal of Geophysical Research: Solid Earth*, *88*(S01), B3–B16. https://doi.org/10.1029/JB088iS01p000B3

Dwyer, C. a., Stevenson, D. J., & Nimmo, F. (2011). A long-lived lunar dynamo driven by continuous mechanical stirring. *Nature*, *479*(7372), 212–214. https://doi.org/10.1038/nature10564

Dygert, N. J., Hirth, G., & Liang, Y. (2016). A flow law for ilmenite in dislocation creep: Implications for lunar cumulate mantle overturn. *Geophysical Research Letters*, *43*(2), 532–540. https://doi.org/10.1002/2015GL066546

Elardo, S. M., Draper, D. S., & Shearer, C. K. (2011). Lunar Magma Ocean crystallization revisited: Bulk composition, early cumulate mineralogy, and the source regions of the highlands Mg-suite. *Geochimica et Cosmochimica Acta*, *75*(11), 3024–3045. https://doi.org/10.1016/j.gca.2011.02.033

Elkins-Tanton, L. T., Burgess, S., & Yin, Q.-Z. (2011). The lunar magma ocean: Reconciling the solidification process with lunar petrology and geochronology. *Earth and Planetary Science Letters*, *304*(3–4), 326–336. https://doi.org/10.1016/j.epsl.2011.02.004

Elkins Tanton, L. T., Van Orman, J. A., Hager, B. H., Grove, T. L., Elkins-Tanton, L. T., Van Orman, J. A., et al. (2002). Re-examination of the lunar magma ocean cumulate overturn hypothesis: Melting or mixing is required. *Earth and Planetary Science Letters*, *196*(3–4), 239–249. https://doi.org/10.1016/S0012-821X(01)00613-6

Evans, A. J., Tikoo, S. M., & Andrews-Hanna, J. C. (2018). The Case Against an Early Lunar Dynamo Powered by Core Convection. *Geophysical Research Letters*, *45*(1), 98–107. https://doi.org/10.1002/2017GL075441

Faul, U. H., & Jackson, I. (2005). The seismological signature of temperature and grain size variations in the upper mantle. *Earth and Planetary Science Letters*, *234*(1–2), 119–134. https://doi.org/10.1016/J.EPSL.2005.02.008

Gagnepain-Beyneix, J., Lognonné, P. H., Chenet, H., Lombardi, D., & Spohn, T. (2006). A seismic model of the lunar mantle and constraints on temperature and mineralogy. *Physics of the Earth and Planetary Interiors*, *159*(3–4), 140–166. https://doi.org/10.1016/j.pepi.2006.05.009

Garcia, R. F., Gagnepain-Beyneix, J., Chevrot, S., & Lognonné, P. H. (2011). Very preliminary reference Moon model. *Physics of the Earth and Planetary Interiors*, *188*(1–2), 96–113. https://doi.org/10.1016/j.pepi.2011.06.015

Garcia, R. F., Gagnepain-Beyneix, J., Chevrot, S., & Lognonné, P. H. (2012). Erratum to " Very Preliminary Reference Moon Model" , by R.F. Garcia, J. Gagnepain-Beyneix, S. Chevrot, P. Lognonne [Phys. Earth Planet. Inter. 188 (2011) 96-113]. *Physics of the Earth and Planetary Interiors*, *202–203*, 89–91. https://doi.org/10.1016/j.pepi.2012.03.009

Ghiorso, M. S., Hirschmann, M. M., Reiners, P. W., & Kress, V. C. (2002). The pMELTS: A revision of MELTS for improved calculation of phase relations and major element partitioning related to partial melting of the mantle to 3 GPa. *Geochemistry, Geophysics, Geosystems*, *3*(5), 1–35. https://doi.org/10.1029/2001GC000217

Green, D. H., Ringwood, A. E., Hibberson, W. O., & Ware, N. G. (1975). Experimental petrology of Apollo 17 mare basalts. *In: Lunar Science Conference*, *1*, 871–893.

Harada, Y., Goossens, S., Matsumoto, K., Yan, J., Ping, J., Noda, H., & Haruyama, J. (2014). Strong tidal heating in an ultralow-viscosity zone at the core–mantle boundary of the Moon. *Nature Geoscience*, *7*(8), 569–572. https://doi.org/10.1038/ngeo2211

Hauri, E. H., Saal, A. E., Rutherford, M. J., & Van Orman, J. a. (2015). Water in the Moon's interior: Truth and consequences. *Earth and Planetary Science Letters*, *409*, 252–264. https://doi.org/10.1016/j.epsl.2014.10.053

Head, J. W., Fassett, C. I., Kadish, S. J., Smith, D. E., Zuber, M. T., Neumann, G. a., & Mazarico, E. (2010). Global distribution of large lunar craters: implications for resurfacing and impactor populations. *Science*, *329*(5998), 1504–1507. https://doi.org/10.1126/science.1195050

Herbert, F. (1980). Time-dependent lunar density models. In *Lunar and Planetary Science Conference Proceedings* (Vol. 11, pp. 2015–2030).

Herd, C. D. K. (2008). Basalts as Probes of Planetary Interior Redox State. *Reviews in Mineralogy and Geochemistry*, *68*(1), 527–553. https://doi.org/10.2138/rmg.2008.68.19

Hess, P. C., & Parmentier, E. M. (1995). A model for the thermal and chemical evolution of the Moon's interior: implications for the onset of mare volcanism. *Earth and Planetary Science Letters*, *134*(3–4), 501–514. https://doi.org/10.1016/0012-821X(95)00138-3

Hood, L. L., Mitchell, D. L., Lin, R. P., Acuña, M. H., & Binder, A. B. (1999). Initial measurements of the lunar induced magnetic dipole moment using Lunar Prospector magnetometer data. *Geophys. Res. Letters*, *26*(15), 2327–2330. https://doi.org/10.1029/1999GL900487

Jaumann, R., Hiesinger, H., Anand, M., Crawford, I. A., Wagner, R., Sohl, F., et al. (2012). Geology, geochemistry, and geophysics of the Moon: Status of current understanding. *Planetary and Space Science*, *74*(1), 15–41. https://doi.org/10.1016/j.pss.2012.08.019

Jing, Z., Wang, Y., Kono, Y., Yu, T., Sakamaki, T., Park, C., et al. (2014). Sound velocity of Fe–S liquids at high pressure: Implications for the Moon's molten outer core. *Earth and Planetary Science Letters*, *396*, 78–87. https://doi.org/10.1016/j.epsl.2014.04.015

Jolliff, B. L., Gillis, J. J., Haskin, L. A., Korotev, R. L., & Wieczorek, M. A. (2000). Major lunar crustal terranes: Surface expressions and crust-mantle origins. *Journal of Geophysical Research: Planets*, *105*(E2), 4197–4216. https://doi.org/10.1029/1999JE001103

Jones, J. H., & Delano, J. W. (1989). A three-component model for the bulk composition of the moon. *Geochimica et Cosmochimica Acta*, *53*(2), 513–527. https://doi.org/10.1016/0016-7037(89)90402-X

Vander Kaaden, K. E., Agee, C. B., & McCubbin, F. M. (2015). Density and compressibility of the molten lunar picritic glasses: Implications for the roles of Ti and Fe in the structures of silicate melts. *Geochimica et Cosmochimica Acta*, *149*, 1–20. https://doi.org/10.1016/j.gca.2014.10.029

Kawamura, T., Lognonné, P., Nishikawa, Y., & Tanaka, S. (2017). Evaluation of deep moonquake source parameters: Implication for fault characteristics and thermal state. *Journal of Geophysical Research: Planets*, *122*(7), 1487–1504. https://doi.org/10.1002/2016JE005147

Khan, A., Connolly, J. A. D., Olsen, N., & Mosegaard, K. (2006). Constraining the composition and thermal state of the moon from an inversion of electromagnetic lunar day-side transfer functions. *Earth and Planetary Science Letters*, *248*(3–4), 579–598. https://doi.org/10.1016/j.epsl.2006.04.008

Khan, A., Connolly, J. A. D., Maclennan, J., & Mosegaard, K. (2007). Joint inversion of seismic and gravity data for lunar composition and thermal state. *Geophysical Journal International*, *168*(1), 243–258. https://doi.org/10.1111/j.1365-246X.2006.03200.x

Khan, A., Pommier, A., Neumann, G. A. G. a., & Mosegaard, K. (2013). The lunar moho and the

internal structure of the Moon: A geophysical perspective. *Tectonophysics*, *609*, 331–352. https://doi.org/10.1016/j.tecto.2013.02.024

Khan, A., Connolly, J. A. D., Pommier, A., & Noir, J. (2014). Geophysical evidence formelt in the deep lunar interior and implications for lunar evolution. *Journal of Geophysical Research E: Planets*, *119*(10), 2197–2221. https://doi.org/10.1002/2014JE004661

Konôpková, Z., McWilliams, R. S., Gómez-Pérez, N., & Goncharov, A. F. (2016). Direct measurement of thermal conductivity in solid iron at planetary core conditions. *Nature*, *534*(7605), 99–101. https://doi.org/10.1038/nature18009

Krawczynski, M. J., & Grove, T. L. (2012). Experimental investigation of the influence of oxygen fugacity on the source depths for high titanium lunar ultramafic magmas. *Geochimica et Cosmochimica Acta*, *79*, 1–19. https://doi.org/http://dx.doi.org/10.1016/j.gca.2011.10.043

Kronbichler, M., Heister, T., & Bangerth, W. (2012). High accuracy mantle convection simulation through modern numerical methods. *Geophysical Journal International*, *191*(1), 12–29. https://doi.org/10.1111/j.1365-246X.2012.05609.x

Kuskov, O. L. (1997). Constitution of the Moon: 4. Composition of the mantle from seismic data. *Physics of the Earth and Planetary Interiors*, *102*(3), 239–257. https://doi.org/10.1016/S0031-9201(96)03259-1

Kuskov, O. L., & Kronrod, V. A. (1998). Constitution of the Moon: 5. Constraints on composition, density, temperature, and radius of a core. *Physics of the Earth and Planetary Interiors*, *107*(4), 285–306. https://doi.org/10.1016/S0031-9201(98)00082-X

Laneuville, M., Wieczorek, M. A., Breuer, D., Aubert, J., Morard, G., & Rückriemen, T. (2014). A long-lived lunar dynamo powered by core crystallization. *Earth and Planetary Science Letters*, *401*, 251–260. https://doi.org/10.1016/j.epsl.2014.05.057

Laneuville, M., Taylor, J. H. P., Wieczorek, M. A., & Taylor, G. J. (2018). Distribution of Radioactive Heat Sources and Thermal History of the Moon. *Journal of Geophysical Research: Planets*, *123*(12), 3144–3166. https://doi.org/10.1029/2018JE005742

Langseth, M. G., Clark, S., Chute, J., Keihm, S., & Wechsler, A. (1971). The Apollo 15 Lunar Heat-flow Measurement. *Conference on Lunar Geophysics, Lunar Science Institute*, 390–410.

Langseth, M. G., Keihm, S. J., & Peters, K. (1976). Revised lunar heat-flow values. *Lunar Science Conference, 7th*, 3143–3171.

Li, H., Zhang, N., Liang, Y., Wu, B., Dygert, N. J., Huang, J., & Parmentier, E. M. (2019). Lunar Cumulate Mantle Overturn: A Model Constrained by Ilmenite Rheology. *Journal of Geophysical Research: Planets*, *0*(ja), 2018JE005905-2018JE005905. https://doi.org/10.1029/2018JE005905

Lin, Y., Tronche, E. J., Steenstra, E. S., & van Westrenen, W. (2017a). Evidence for an early wet Moon from experimental crystallization of the lunar magma ocean. *Nature Geosci*, *10*(1), 14–18. https://doi.org/10.1038/ngeo2845 http://www.nature.com/ngeo/journal/v10/n1/abs/ngeo2845.html#supplementary-information

Lin, Y., Tronche, E. J., Steenstra, E. S., & van Westrenen, W. (2017b). Experimental constraints on the solidification of a nominally dry lunar magma ocean. *Earth and Planetary Science*

Letters, *471*, 104–116. https://doi.org/https://doi.org/10.1016/j.epsl.2017.04.045

Lognonné, P. H., & Johnson, C. L. (2007). Planetary Seismology. *Treatise on Geophysics*, *17*(7), 69–122. https://doi.org/10.1029/RG017i007p01641

Mallik, A., Ejaz, T., Shcheka, S., & Garapic, G. (2019). A petrologic study on the effect of mantle overturn: Implications for evolution of the lunar interior. *Geochimica et Cosmochimica Acta*, *250*, 238–250. https://doi.org/10.1016/j.gca.2019.02.014

Matsuyama, I., Nimmo, F., Keane, J. T., Chan, N. H., Taylor, G. J., Wieczorek, M. A., et al. (2016). GRAIL, LLR, and LOLA constraints on the interior structure of the Moon. *Geophysical Research Letters*, *43*(16), 8365–8375. https://doi.org/10.1002/2016GL069952

Morgan, J. W., Hertogen, J., & Anders, E. (1978). The Moon: Composition determined by nebular processes. *The Moon and the Planets*, *18*(4), 465–478. https://doi.org/10.1007/bf00897296

Morrison, D. A. (1998). Did a Thick South Pole-Aitken Basin Melt Sheet Differentiate to Form Cumulates? *29th Annual Lunar and Planetary Science Conference*.

Nakamura, Lammlein, Latham, G. V., Ewing, Dorman, Press, et al. (1973). New Seismic Data on the State of the Deep Lunar Interior. *Science*, *181*(4094), 49–51. https://doi.org/10.1126/science.181.4094.49

Nakamura, Y. (2005). Farside deep moonquakes and deep interior of the Moon. *Journal of Geophysical Research*, *110*(E1), 1–12. https://doi.org/10.1029/2004JE002332

Nakamura, Y., Latham, G. V., Dorman, H. J., Ibrahim, A. K., Koyama, J., & Horvath, P. (1978). Shallow Moonquakes: Depth, Distribution, and Implications as to the Present State of the Lunar Interior. *Proc. Lunar Planet. Sci. Conf. 9th*, 2299–2309.

Neal, C. R. (2009). The Moon 35 years after Apollo: What's left to learn? *Chemie Der Erde*, *69*(1), 3–43. https://doi.org/10.1016/j.chemer.2008.07.002

Nimmo, F., Faul, U. H., & Garnero, E. J. (2012). Dissipation at tidal and seismic frequencies in a melt-free Moon. *Journal of Geophysical Research*, *117*(E9), E09005. https://doi.org/10.1029/2012JE004160

O'Neill, H. S. C. (1991). The origin of the moon and the early history of the earth—A chemical model. Part 1: The moon. *Geochimica et Cosmochimica Acta*, *55*(4), 1135–1157. https://doi.org/10.1016/0016-7037(91)90168-5

Van Orman, J. A., & Grove, T. L. (2000). Origin of lunar high-titanium ultramafic glasses: Constraints from phase relations and dissolution kinetics of clinopyroxene-ilmenite cumulates. *Meteoritics & Planetary Science*, *35*(4), 783–794. https://doi.org/10.1111/j.1945-5100.2000.tb01462.x

Price, K. V., Storn, R. M., Lampinen, J. A., & SpringerLink (Online service). (2005). *Differential evolution a practical approach to global optimization*. *Natural computing series,*. Springer.

Righter, K., Go, B. M. M., Pando, K. A. A., Danielson, L., Ross, D. K. K., Rahman, Z., & Keller, L. P. P. (2017). Phase equilibria of a low S and C lunar core: Implications for an early lunar dynamo and physical state of the current core. *Earth and Planetary Science Letters*, *463*, 323–332. https://doi.org/10.1016/j.epsl.2017.02.003

Ringwood, A. E. (1979). Geochemistry of the Moon. In *Origin of the Earth and Moon* (pp. 198–

228). New York, NY: Springer New York. https://doi.org/10.1007/978-1-4612-6167-4_11

Ringwood, A. E., & Kesson, S. E. (1976). Limits on the Bulk Composition on the Moon. *Seventh Lunar Science Conference*. Houston: Lunar and Planetary Institute.

Ringwood, A. E., & Kesson, S. E. (1977). Basaltic magmatism and the bulk composition of the moon. *The Moon*, *16*(4), 425–464. https://doi.org/10.1007/bf00577902

Ringwood, A. E., Seifert, S., & Wänke, H. (1987). A komatiite component in Apollo 16 highland breccias: implications for the nickel-cobalt systematics and bulk composition of the moon. *Earth and Planetary Science Letters*, *81*(2), 105–117. https://doi.org/10.1016/0012-821X(87)90149-X

Sakamaki, T., Ohtani, E., Urakawa, S., Suzuki, A., Katayama, Y., & Zhao, D. (2010). Density of high-Ti basalt magma at high pressure and origin of heterogeneities in the lunar mantle. *Earth and Planetary Science Letters*, *299*(3–4), 285–289. https://doi.org/10.1016/j.epsl.2010.09.007

Shea, E. K., Weiss, B. P., Cassata, W. S., Shuster, D. L., Tikoo, S. M., Gattacceca, J., et al. (2012). A long-lived lunar core dynamo. *Science (New York, N.Y.)*, *335*(6067), 453–6. https://doi.org/10.1126/science.1215359

Shimizu, H., Matsushima, M., Takahashi, F., Shibuya, H., & Tsunakawa, H. (2013). Constraint on the lunar core size from electromagnetic sounding based on magnetic field observations by an orbiting satellite. *Icarus*, *222*(1), 32–43. https://doi.org/10.1016/j.icarus.2012.10.029

Snyder, G. A., Taylor, L. A., & Neal, C. R. (1992). A chemical model for generating the sources of mare basalts: Combined equilibrium and fractional crystallization of the lunar magmasphere. *Geochimica et Cosmochimica Acta*, *56*(10), 3809–3823. https://doi.org/10.1016/0016-7037(92)90172-F

Steenstra, E. S., Rai, N., Knibbe, J. S., Lin, Y. H., & van Westrenen, W. (2016). New geochemical models of core formation in the Moon from metal-silicate partitioning of 15 siderophile elements. *Earth and Planetary Science Letters*, *441*, 1–9. https://doi.org/10.1016/j.epsl.2016.02.028

Stegman, D. R., Jellinek, a M., Zatman, S. a, Baumgardner, J. R., & Richards, M. a. (2003). An early lunar core dynamo driven by thermochemical mantle convection. *Nature*, *421*(6919), 143–6. https://doi.org/10.1038/nature01267

Stevenson, D. J. (1980). Lunar asymmetry and palaeomagnetism. *Nature*, *287*(5782), 520–521. https://doi.org/10.1038/287520a0

Stevenson, D. J., & Halliday, A. N. A. N. (2014). The origin of the Moon. *Philosophical Transactions of the Royal Society A: Mathematical, Physical and Engineering Sciences*, *372*(2024), 20140289. https://doi.org/10.1098/rsta.2014.0289

Taylor, S. R. (1980). Refractory and moderately volatile element abundances in the earth, moon and meteorites. In *Lunar and Planetary Science Conference Proceedings* (Vol. 11, pp. 333–348).

Taylor, S. R. (1982). *Planetary Science: A Lunar Perspective*. Houston: Lunar and Planetary Institute.

Taylor, S. R. (1999). The Moon. In P. R. Weissman, L.-A. McFadden, & T. V Johnson (Eds.), *Encyclopedia of the Solar System* (pp. 247–276). Academic Press.

Taylor, S. R., & Bence, A. E. (1975). Evolution of the lunar highland crust. In *Lunar and Planetary Science Conference Proceedings* (Vol. 6, pp. 1121–1141).

Tian, Z. L., Wisdom, J., & Elkins-Tanton, L. T. (2017). Coupled orbital-thermal evolution of the early Earth-Moon system with a fast-spinning Earth. *Icarus*, *281*, 90–102. https://doi.org/10.1016/j.icarus.2016.08.030

Tikoo, S. M., Weiss, B. P., Cassata, W. S., Shuster, D. L., Gattacceca, J., Lima, E. a., et al. (2014). Decline of the lunar core dynamo. *Earth and Planetary Science Letters*, *404*, 89–97. https://doi.org/10.1016/j.epsl.2014.07.010

Tikoo, S. M., Weiss, B. P., Shuster, D. L., Suavet, C., Wang, H., & Grove, T. L. (2017). A two-billion-year history for the lunar dynamo. *Science Advances*, *3*(8), 1–9. https://doi.org/10.1126/sciadv.1700207

Touma, J., & Wisdom, J. (1994). Evolution of the Earth-Moon system. *The Astronomical Journal*, *108*, 1943–1961.

de Vries, J., van den Berg, A., & van Westrenen, W. (2010). Formation and evolution of a lunar core from ilmenite-rich magma ocean cumulates. *Earth and Planetary Science Letters*, *292*(1–2), 139–147. https://doi.org/10.1016/j.epsl.2010.01.029

Wagner, T. P., & Grove, T. L. (1997). Experimental constraints on the origin of lunar high-Ti ultramafic glasses. *Geochimica et Cosmochimica Acta*, *61*(6), 1315–1327. https://doi.org/10.1016/S0016-7037(96)00387-0

Wänke, H., & Dreibus, G. (1982). Chemical and Isotopic Evidence for the Early History of the Earth-Moon System. In P. Brosche & J. Sündermann (Eds.), *Tidal Friction and the Earth's Rotation II: Proceedings of a Workshop Held at the Centre for Interdisciplinary Research (ZiF) of the University of Bielefeld, September 28–October 3, 1981* (pp. 322–344). Berlin, Heidelberg: Springer Berlin Heidelberg. https://doi.org/10.1007/978-3-642-68836-2_19

Wänke, H., & Dreibus, G. (1986). Geochemical evidence for the formation of the Moon by impact-induced fission of the proto-Earth. *Origin of the Moon*, 649.

Wänke, H., Baddenhausen, H., Blum, K., Cendales, M., Dreibus, G., Hofmeister, H., et al. (1977). On the chemistry of lunar samples and achondrites-Primary matter in the lunar highlands: A re-evaluation. In *Lunar and Planetary Science Conference Proceedings* (Vol. 8, pp. 2191–2213).

Warren, P. H. (2005). "New" lunar meteorites: Implications for composition of the global lunar surface, lunar crust, and the bulk Moon. *Meteoritics & Planetary Science*, *40*(3), 477–506. https://doi.org/10.1111/j.1945-5100.2005.tb00395.x

Warren, P. H., & Dauphas, N. (2014). Revised Estimation of the Bulk Composition of the Moon in Light of GRAIL Results, and Why Heat Flow Should be a Top Priority for Future Lunar Missions. In *Lunar and Planetary Science Conference* (Vol. 45, p. 2298).

Weber, R. C., Lin, P.-Y., Garnero, E. J., Williams, Q. C., & Lognonné, P. H. (2011). Seismic Detection of the Lunar Core. *Science*, *331*(6015), 309–312. https://doi.org/10.1126/science.1199375

Weiss, B. P., & Tikoo, S. M. (2014). The lunar dynamo. *Science*, *346*(6214), 1246753–1246753. https://doi.org/10.1126/science.1246753

Wieczorek, M. A., Jolliff, B. L., Khan, A., Pritchard, M. E., Weiss, B. P., Williams, J. G., et al.

(2006). The Constitution and Structure of the Lunar Interior. *Reviews in Mineralogy & Geochemistry*, *60*(1), 221–364. https://doi.org/10.2138/rmg.2006.60.3

Wieczorek, M. A., Neumann, G. a., Nimmo, F., Kiefer, W. S., Taylor, G. J., Melosh, H. J., et al. (2013). The crust of the Moon as seen by GRAIL. *Science (New York, N.Y.)*, *339*(6120), 671–5. https://doi.org/10.1126/science.1231530

Williams, J. G., Boggs, D. H., Yoder, C. F., Ratcliff, J. T., & Dickey, J. O. (2001). Lunar rotational dissipation in solid body and molten core. *Journal of Geophysical Research*, *106*(E11), 27933. https://doi.org/10.1029/2000JE001396

Yan, J., Xu, L., Li, F., Matsumoto, K., Rodriguez, J. A. P., Miyamoto, H., & Dohm, J. M. (2015). Lunar core structure investigation: Implication of GRAIL gravity field model. *Advances in Space Research*, *55*(6), 1721–1727. https://doi.org/10.1016/j.asr.2014.12.038

Yang, H., & Zhao, W. (2015). Improved Views of the Moon in the Early Twenty First Century: A Review. *Earth, Moon, and Planets*, *114*(3–4), 101–135. https://doi.org/10.1007/s11038-015-9459-9

Yao, L., & Liang, Y. (2012). The search for the lunar core. *Lunar and Planetary Science Conference 43rd*, 1–2.

Yu, S., Tosi, N., Schwinger, S., Maurice, M., Breuer, D., & Xiao, L. (2019). Overturn of ilmenite-bearing cumulates in a rheologically weak lunar mantle. *Journal of Geophysical Research: Planets*, *0*(ja). https://doi.org/10.1029/2018JE005739

Zhao, Y., de Vries, J., van den Berg, A. P., Jacobs, M. H. G., & van Westrenen, W. (2019). The participation of ilmenite-bearing cumulates in lunar mantle overturn. *Earth and Planetary Science Letters*, *511*, 1–11. https://doi.org/https://doi.org/10.1016/j.epsl.2019.01.022

Zhang, B., Ge, J., Xiong, Z., Zhai, S., 2019. Effect of Water on the Thermal Properties of Olivine With Implications for Lunar Internal Temperature. J. Geophys. Res. Planets 124, 3469–3481. https://doi.org/10.1029/2019JE006194

Zhong, S., Parmentier, E. M., & Zuber, M. T. (2000). A dynamic origin for the global asymmetry of lunar mare basalts. *Earth and Planetary Science Letters*, *177*(3–4), 131–140. https://doi.org/10.1016/S0012-821X(00)00041-8